

THESIS FOR THE DEGREE OF LICENTIATE OF ENGINEERING

Characterization of Electrodeposited Fe-based Metallic Coatings:  
Toward a Sustainable Approach

Antonio Mulone

Department of Industrial and Materials Science  
CHALMERS UNIVERSITY OF TECHNOLOGY

Gothenburg, Sweden 2018

Characterization of Electrodeposited Fe-based Metallic Coatings: Toward a Sustainable Approach

ANTONIO MULONE

© ANTONIO MULONE, 2018.

Technical report no IMS-2018-5  
Department of Industrial and Materials Science  
Chalmers University of Technology  
SE-412 96 Gothenburg  
Sweden  
Telephone + 46 317721268

Printed by Chalmers Reproservice  
Gothenburg, Sweden 2018

# Characterization of Electrodeposited Fe-based Metallic Coatings: Toward a Sustainable Approach

ANTONIO MULONE

Department of Industrial and Materials Science  
Chalmers University of Technology

## Abstract

Electrodeposition has rapidly grown in the last 50 years and it has been applied to deposit metals and alloys with complex shapes or to produce fully dense nanostructures and amorphous coatings. Thanks to the achieved improved properties of the electrodeposited materials, electrodeposition has been applied in a wide set of applications including protective coatings, and magnetic and electronic applications. The integration of sustainability with technological progress has become one of the major challenges in our modern society. To fulfil this important goal within the area of electrodeposited materials, it is of major importance to develop innovative metallic coatings deposited with a sustainable approach. This means the use of environmental-friendly electrolytic baths for the deposition of properly designed alloys without or with minimum amounts of scarce or toxic elements.

This work deals with the characterization of Fe-based metallic coatings electrodeposited with a sustainable approach. Characterization studies have been performed on Fe-W coatings and Sn coatings. The study on the Sn coatings has been performed as a preliminary investigation to be then followed up by the deposition and characterization of binary and ternary Fe-Sn coatings. Different techniques such as Scanning Electron Microscopy (SEM), Electron Back Scatter Diffraction (EBSD), Transmission Electron Microscopy (TEM), X-ray Diffraction (XRD), Glow Discharge Optical Emission Spectroscopy (GD-OES), and Nanoindentation were used to characterize the structure and the properties of the coatings.

It was found that the as-deposited structure of the Fe-W coatings changes with increase of the W content: a nanocrystalline, a mixed nanocrystalline-amorphous, and a fully amorphous structure was found when raising the W content from 4 up to 24 at.%. The thermal stability of Fe-W alloys increases with the W content, i.e. the Fe-W sample with 24 at.% W retains the amorphous structure up to 600 °C. Co-deposited C and O impurities in the coatings lead upon annealing to the formation of phase not expected from the Fe-W diagram:  $\text{Fe}_6\text{W}_6\text{C}$ ,  $\text{Fe}_3\text{W}_3\text{C}$ , and  $\text{FeWO}_4$  phases. Longer annealing treatments resulted in the gradual dissolution of the carbide phases and the crystallization of the  $\text{Fe}_2\text{W}$  phase. The annealing treatments improved considerably the hardness of the as-deposited Fe-W samples. The maximum hardness of 16.5 GPa was measured for the sample with 24 at.% of W after annealing for one hour at 600 °C. Sn coatings were deposited from two different electrolytes, i.e. a chloride-based and a methane sulfonic acid (MSA) electrolyte. It was found that the additive used acts as a highly effective inhibitor in the chloride-based electrolyte. Its addition lead to a decrease in the limiting current density, suppression of  $\text{H}_2$  evolution, and to changes in the grain structure of the deposited Sn samples. The same effects are not observed in the MSA electrolyte.

**Keywords:** Electrodeposition, coatings, iron alloys, electrodeposited tin, structural characterization



## Preface

This licentiate thesis is based on the work performed at the Department of Industrial and Materials Science between September 2015 and February 2018 under the supervision of Professor Uta Klement. This research was funded by the European Union's Horizon 2020 research and innovation program under the Marie Skłodowska-Curie grant agreement No 642642 (SELECTA). Part of the experimental work was performed in collaboration with Aliona Nicolenco, PhD student at Vilnius University, and Simona Zajkoska, industrial PhD student at Hirtenberger Engineered Surfaces GmbH and University of Vienna. The thesis consists of seven chapters of introduction and the following appended papers:

- Paper 1:** In-depth characterization of as-deposited and annealed Fe-W coatings electrodeposited from glycolate-citrate plating bath  
A. Mulone, A. Nicolenco, V. Hoffmann, U. Klement, N. Tsyntsaru, H. Cesiulis  
*Electrochimica Acta*, Vol. 261 (2018), pp. 167-177
- Paper 2:** The effect of heat treatment on the structure and on the hardness of Fe-W alloys electrodeposited from a glycolate-citrate plating bath  
A. Mulone, A. Nicolenco, J. Fornell, E. Pellicer, N. Tsyntsaru, H. Cesiulis, J. Sort, U. Klement  
In manuscript
- Paper 3:** Alkoxyated  $\beta$ -naphthol as an additive for tin plating from chloride and methane sulfonic acid electrolytes.  
S. Zajkoska, A. Mulone, W. Hansal, U. Klement, R. Mann, W. Kautek  
*Coatings*, Vol. 8(2) (2018), 79

## Contribution to the appended papers

- Paper 1:** I conducted most of the experimental work, i.e. SEM, XRD and annealing treatments. TEM analysis were performed together with Dr. Yiming Yao. The GD-OES measurements were performed by PhD student Aliona Nicolenco together with Dr. V. Hoffman from IFW Dresden. The paper was written in collaboration with the co-authors.
- Paper 2:** I planned and conducted the experimental work and wrote the paper in collaboration with the co-authors. The nanoindentation measurements were performed at the Department de Física of the Universitat Autònoma de Barcelona in collaboration with Dr. Jordina Fornell, Dr. Eva Pellicer and Prof. Jordi Sort
- Paper 3:** I planned and conducted the structural characterization of the samples and wrote the paper in collaboration with the co-authors. The electrochemical characterization was performed by PhD student Simona Zajkoska.



## Table of Contents

1	Introduction.....	2
1.1	Electrodeposition with a sustainable approach.....	2
1.2	Research objectives .....	3
1.3	Limitations.....	4
2	Background.....	5
2.1	Electrodeposition: the setup.....	5
2.2	Deposition parameters and their influence on the deposition process.....	7
2.3	Electrocrystallization: growth mode and microstructure.....	7
2.4	Nanocrystalline and amorphous electrodeposits .....	10
3	Analyzed materials and deposition method .....	12
3.1	Previous studies on Fe-W electrodeposits .....	12
3.2	Electrodeposition of Fe-W alloys .....	12
3.3	Previous studies on electrodeposited Sn.....	14
3.4	Electrodeposition of Sn .....	15
4	Characterization techniques .....	16
4.1	Imaging techniques.....	16
4.1.1	Scanning Electron Microscopy (SEM) .....	16
4.1.2	Electron Back Scatter Diffraction (EBSD) .....	17
4.1.3	Transmission Electron Microscopy (TEM).....	18
4.2	Non-imaging techniques.....	19
4.2.1	X-ray diffraction (XRD).....	19
4.2.2	Glow discharge optical emission spectroscopy (GD-OES) .....	20
4.2.3	Nanohardness measurements .....	20
5	Summary of results and discussions .....	22
5.1	Characterization of electrodeposited Fe-W alloys.....	22
5.1.1	Interdependences between the composition, the structure and the thermal stability of Fe-W coatings.....	22
5.1.2	Heat treatment effects on the hardness and on the microstructure of Fe-W coatings .....	23
5.2	Characterization of electrodeposited Sn .....	26
5.2.1	Alkoxylated $\beta$ -naphthol additive effects on the deposition of Sn .....	26
5.2.2	Additive effects on the Sn morphology and crystallographic orientation.....	27
6	Summary and Conclusions .....	30
7	Future work.....	32

8	Acknowledgment .....	33
9	References .....	34

# 1 Introduction

As defined by the standards, electrodeposition is a technology for the deposition of a material on an electrode for the purpose of securing a surface with properties or dimensions different from those of the substrate [1]. This technique can be used to deposit different materials, including metal matrix composites, oxides and semiconductors, but it is commonly applied to deposit metals and alloys [2]. The growth of the metallic coating occurs through the electrochemical reduction of the metal ions from an electrolyte [3]. Some of the main advantages of this deposition technique are the simplicity of implementation, the low capital cost needed, and the high process versatility. Thanks to such characteristics, this technique has been used since the nineteenth century for the deposition of decorative films in jewelry and luxury items, and for the production of coatings with improved mechanical or wear properties as well as coatings providing corrosion resistance [3]. In the last 50 years, electrodeposition has rapidly grown and thanks to an increased understanding of its fundamentals, it has been applied to deposit metals and alloys with complex shapes (i.e. films, micropillars, nanowires) and to produce fully dense nanostructures and amorphous coatings by properly tuning the microstructure of the deposited material [3,4]. Thus, thanks to the achieved improved properties of the electrodeposited materials, electrodeposition has been applied in a wider set of applications, including magnetic and electronic applications [5,6].

## 1.1 Electrodeposition with a sustainable approach

Our modern society is built on the need of a continuous technological and economic growth. But there is the risk to reach a critical point in which the availability of natural resources will no longer be sufficient to answer the increasing demand of technological advances [7]. For this reason, the integration of sustainability with technological progress is becoming one of the major challenges in modern society [8]. Reaching this goal within the area of electrodeposition is of major importance and it represents a true challenge. As a matter of fact, scarce or toxic substances are still widely used for the deposition of coatings which are dominating in most of the electrodeposition applications, i.e. protective coatings, and magnetic and electronic applications. Hard chromium and cadmium are commonly used as protective coatings thanks to their excellent properties of wear and corrosion resistance, but their electrodeposition involves the use of highly cancerogenic substances (e.g. hexavalent chromium and cadmium salts) [9]. Proposed material alternatives such as NiW, NiP and CoW coatings [10] do not represent a valid choice as both Co and Ni are targeted as hazardous in most recent environmental legislations [9], and P being named as an essential non-replaceable nutrient but available with limited supplies [11]. Rare-earth and noble-metal, are present in the list of critical raw material created from the European Commission [12]. As a matter of fact, most of the reserves of rare-earth metals are found in China and Russia. Sustainable production and consumption is also one of the 17 UN goals adopted in 2015 for a sustainable development [13], see Fig. 1. Here, one of the main targeted goals is to achieve a sustainable management and efficient use of natural resources.

To face these issues, the European Training Network SELECTA (Smart ELECTrodeposited Alloys for environmentally sustainable applications: from advanced protective coatings to micro/nano- robotic platforms) was launched in January 2015 with the goal to integrate technological progress with environmental sustainability concerns [8,14]. The project aims to develop a “green” electrochemical synthesis for innovative metallic alloys to be implemented

in the above mentioned applications, i.e. advanced protective coatings and electromechanical and magnetic systems (MEMS/NEMS).



Figure 1: The 17 goals for a sustainable development, inspired from [13].

The adopted sustainable approach to achieve this goal comprises the use of environmental-friendly and minimally invasive electrolytic baths for the deposition of properly designed alloys (based on Fe, Cu or Al) without or with minimum amounts of scarce or toxic elements [14]. In this perspective the four following compositional restrictions are applied:

- Restriction 1: Avoid rare-earth and noble metals
- Restriction 2: Avoid highly toxic metals
- Restriction 3: Avoid use of cobalt or nickel
- Restriction 4: Minimize use of gallium and phosphorus

## 1.2 Research objectives

Within the scope of the SELECTA project, this research focuses on the characterization of electrodeposited Fe-based metallic coatings. Specifically, characterization studies have been performed on Fe-W coatings deposited from an environmental friendly Fe(III)-based glycolate-citrate bath. Such coatings aim to be applied as protective coating for hard chromium replacement. Furthermore, Sn coatings electrodeposited from a chloride and from methane sulfonic acid (MSA) based electrolytes have also been studied. Particular attention was put on studying the effects of the organic additive used for Sn electrodeposition. The characterization of the Sn coatings has been performed as a preliminary investigation to be then followed up by the deposition of binary and ternary Fe-Sn coatings for MEMS applications.

The research objectives can be divided depending on the coating under investigation as follows:

1. The composition and structure of electrodeposited Fe-W alloys is influenced by the applied electrodeposition conditions. The possibility to tune the material structure represents a useful opportunity when aiming for certain properties of interest. For

protective coating applications, properties of interest are e.g. hardness, thermal stability, and wear and corrosion resistance. Hence, the aim of this work is to study the interdependences between the composition and structure of Fe-W coatings by using adequate characterization techniques. The analysis is then extended to the influences of the structure and composition on the material properties, like hardness and thermal stability. Furthermore, the possibility to optimize the hardness of the materials by proper annealing treatments is also studied.

2. Organic additives are needed for the deposition of homogenous and compact tin coatings from acidic solutions. One of the first additives introduced to tin electroplating electrolytes was  $\beta$ -naphthol. The aim of this work is to investigate the influence of alkoxyated  $\beta$ -naphthol (ABN), which is more stable against oxidation than  $\beta$ -naphthol, on the electrodeposition of tin. Specifically, the effect of the additive on the kinetic behavior of the used electrolytes and on the structure of the deposited Sn coatings is studied.

Therefore, the research questions are the following:

- When electrodepositing Fe-W alloys, what is the influence of the W content and of co-deposited impurities on the structure of the coatings?
- How are composition and structure influencing the hardness and thermal stability of the Fe-W coatings?
- Are the properties of the Fe-W coatings suitable for protective coating applications and other potential applications?
- When electrodepositing Sn coatings, what is the influence of ABN additive on the two different electrolytes, i.e. chloride and MSA electrolytes?

### 1.3 Limitations

This work is concerning the structural characterization of the electrodeposited Fe-W and Sn coatings. The investigated coatings were not deposited by the author. The Fe-W coatings were deposited by the PhD student Aliona Nicolenco at the University of Vilnius (Lithuania). The Sn coatings were deposited by the PhD student Simona Zajkoska at Hirtenberger Engineered Surface GmbH (Austria). The results concerning the deposition process and the electrochemical characterization of the materials are included and linked to the results from the structural characterization of the coatings. This is done in order to outline the possible interdependences between the applied deposition conditions and the material microstructure. This work is not aiming at investigating the influence of the deposition parameters on the electrochemical thermodynamics of the deposition process. Hence, a detailed discussion of the applied deposition parameters and of the electrochemical characterization is not provided.

## 2 Background

In this chapter, a brief overview of the electrodeposition process including the electrodeposition set up and some of the electrodeposition fundamental concepts are provided. Also, the concept of electrocrystallization and of nanocrystalline and amorphous electrodeposits are introduced.

### 2.1 Electrodeposition: the setup

The necessary components present in the electrodeposition setup are the following: (i) the electrode to be coated, referred usually as cathode or working electrode, (ii) an electrolyte containing the ions of the material to deposit, (iii) an anode or counter electrode, and (iv) an external power supply, i.e. current or voltage. The object to be coated is connected to the negative terminal of the power supply. In this way, the dissolved metal ions are reduced to metal atoms, which eventually will form a coating on the surface of the working electrode [3]. The overall process is shown in the schematic representation in Fig. 2.

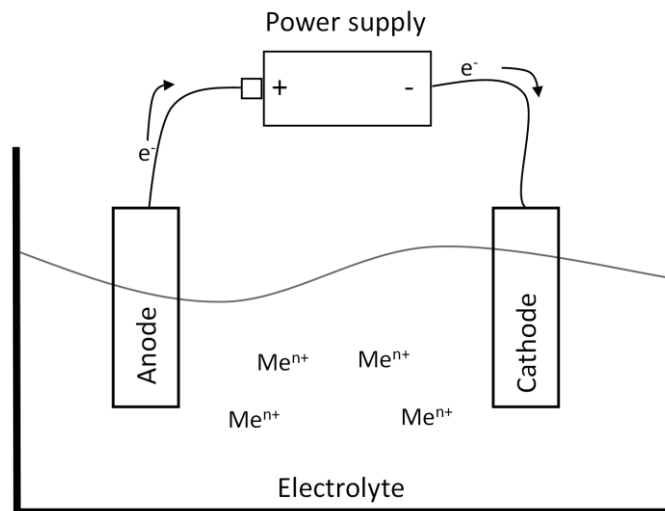


Figure 2: Schematic representation of the setup for an electrodeposition process.

Depending on the type of input provided by the external power supply, it is possible to refer to a galvanostatic process when a constant current is applied while the potential is changing over time. A potentiostatic process is obtained when the constant potential difference applied is accompanied by variations of the current. The relationship between the amount of deposited material and the external current applied is described by Faraday's law [3]:

$$m = QA/nF$$

Where  $m$  is the mass of the deposited metal,  $Q$  is the net charge applied to the system,  $A$  is the atomic weight of the metal,  $n$  the number of electrons transferred during the deposition process, and  $F$  is the Faraday constant. Under the assumption of a constant current applied ( $Q=I\tau$ , where  $I$  is the current and  $\tau$  the duration of the electrolysis), the Faraday's law can be expressed as the dependence of the deposit thickness  $h$  ( $h=m/S\rho$ , where  $S$  is the surface area and  $\rho$  is the density) upon the duration of the electrolysis and the applied current density  $j$  (where  $j=I/S$ ) [3]:

$$h = jA\tau/dnF$$

However, in an electrodeposition process, part of the overall current applied is consumed by side reactions occurring in parallel with the metal deposition, e.g. hydrogen evolution. The current efficiency of the deposition process is thus given by the ratio of the actual deposited mass,  $\Delta m$ , to its theoretical value calculated from the Faraday's law [3]:

$$CE = \Delta m / QA / n F$$

Electrodeposition of metals and alloys is commonly performed by using an aqueous solution as electrolyte. Simple water based electrolytes contain salts or other soluble compounds having the metal in the form of cationic or anions metal complexes. Inorganic acids or alkali are also added to improve the conductivity of the solution and to stabilize the metal complexes of interests. In addition, different organic substances, known as additives, can be added to the used electrolyte for various reasons. Among the different additives the most common are: (i) surfactants, added to decrease the surface energy of the electrode and to “block” the high-energy surface sites slowing down the electrodeposition, (ii) grain-refiners, added to make the deposited metal surface smooth, (iii) brighteners, added to obtain a bright finish deposit, and (iv) levelers, added to fill pre-existing scratches or voids in the surface of the electrode [3,15]. These organic substances are added into the electrolytic bath to hinder the cathodic process, i.e. the reduction of the metal ions. The reduction process is hindered because the additives are physically/chemically absorbed mostly on the electrode surface active sites, like surface defect sites, and for this are called inhibitors. In fact, according to Fischer [16], in electrodeposition inhibition is occurring due to the presence of substances at the surface of the substrate which are different from the metallic species to be deposited.

Polarization measurements are commonly performed in order to study the different processes occurring during an electrodeposition process, i.e. the reaction mechanism and the kinetics of metal deposition, the effects of the inhibitors or hydrogen evolution. A polarization curve describes the relationship between the potential and the current during an electrochemical reaction. An experimental polarization curve is obtained by imposing various potential values and by measuring the corresponding value of the current. To perform such measurements a three electrodes set-up which includes a reference electrode is needed. The applied potential to drive the electrochemical reaction is conventionally measured with respect to the reference electrode. Figure 3 shows a schematic representation of a three electrode set up and a representative polarization measurement. The polarization curves shown in Fig. 3b are measured for Sn electrodeposition from a chloride-based electrolyte. The curve with the continuous line is measured in the electrolyte without additive, the curve with the dashed line is measured after adding 3.12 mg/l of ABN. In both the curves shown in Fig 3b, the measured cathodic current density starts to increase at a potential around -700 mV, until a plateau of the current density is reached. The increase in current density before the plateau is associated with the diffusion-limited reduction of Sn(II). For the curve measured without the addition of the additive, a further increase of the current density is observed after the plateau. This is due to hydrogen evolution. The addition of the additive leads to a decrease of the measured cathodic current density and also to a suppression of the hydrogen evolution, as observable from the dashed curve. These effects are typical of additives providing inhibition during the performed electrodeposition.

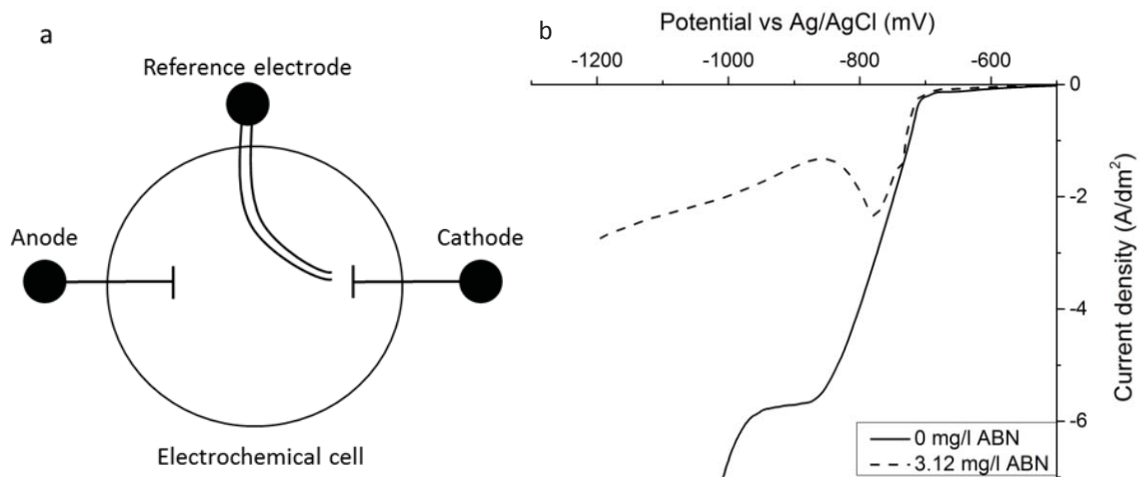


Figure 3: Schematic representation of a three electrode set up (a), and experimental polarization curves measured for Sn electrodeposition from a chloride-based electrolyte (b). The curve with the continuous line is measured in the electrolyte without additive, the curve with the dashed line is measured after adding 3.12 mg/l of ABN.

## 2.2 Deposition parameters and their influence on the deposition process

Beside the current density, the electrode potential and the type of electrolyte used, there are other important parameters which influence the electrodeposition process such as the electrolyte temperature, the pH of the solution, the stirring rate of the solution, and the substrate surface finishing [3]. On one hand high temperatures improve the species solubility and the conductivity of the electrolyte, on the other hand they also lead to faster evaporation of the electrolyte thus limiting the practical temperatures achievable. Coatings deposited at lower temperatures can suffer from internal stresses and may be prone to embrittlement. The pH value of the electrolyte influences the stability and distribution of metallic species in the electrolyte, side reactions such as hydrogen evolution, and the current efficiency of the deposition process. Stirring of the solution, usually performed by magnetic stirrers, enhances the ion transport from the electrolyte to the surface of the substrate, but can also reduce the coating adhesion. The substrate surface finishing influences the growth process of the deposited films, especially in the initial stages. A smooth surface has a minimal impact on the growth of the film, while surface pre-treatments, such as chemical etching, increase the influence on the growing film.

## 2.3 Electrocrystallization: growth mode and microstructure

With respect to the deposition of a metallic coating, all the electrodeposition processes have in common the transfer of one or more electrons through the electrode/solution interface. The overall process can be divided in three main steps [3]. The first step represents the mass transfer of the species to be reduced to the surface of the electrode. Here, as a second step, charge transfer occurs and the reduced metal atom adsorbs at the electrode surface. In the last step, the adsorbed metal atom (also defined as adion) can diffuse across the surface to active growth sites, i.e. a surface defect such as a kink site or an atomic step [17], where it is incorporated into the crystal lattice of the deposit. In Fig. 4 is provided a schematic representation of the three described steps and of the surface growth sites.

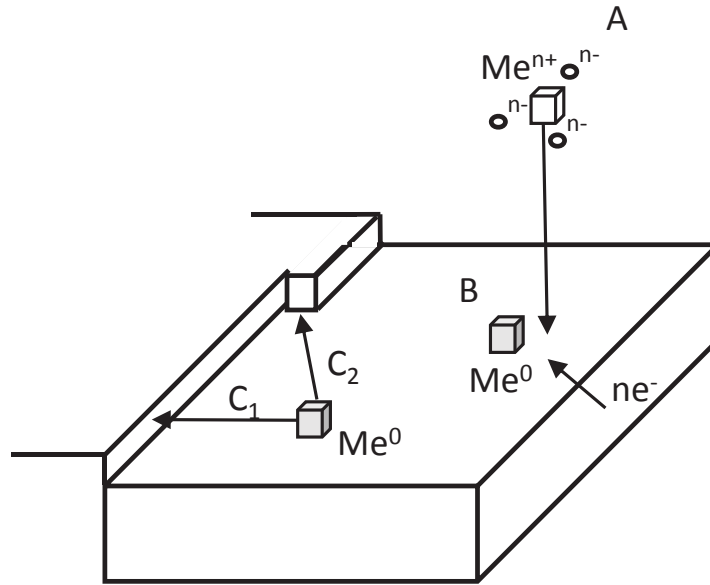


Figure 4: Schematic representation of the three main steps of an electrocrystallization process: mass transfer of the active species (A), charge transfer between adion and the substrate (B), diffusion of adion to an active growth site like an atomic step ( $C_1$ ) or a kink site ( $C_2$ ). In step A, the particles with the negative charge are representing ligands from the electrolyte.

The adsorbed adions diffuse to active sites because in those sites they are more stably bound to the substrate. After the neutralization step through the charge transfer (step B in Fig. 4), an adion is neither completely discharged nor completely de-solvated [17]. It still carries remaining ligands from the electrolyte with an opposite charge. An adion adsorbed in a step or kink position is less hydrated than a corresponding adion adsorbed in free-surface site. Hence, the bonding to the substrate in a step and in a kink site is stronger.

The growth mode of the electrodeposited metal can proceed according to different models [18]. In the case of electrodeposition occurring at a surface with a high density of growth sites (i.e. kink and step sites) and with low inhibition (using a bath without additives or with low amounts), the discharge and attachment of atoms to the lattice occurs across the whole surface forming isolated “island” nuclei which will afterwards grow vertically. This is referred to as island growth or normal growth mode [3,15]. The deposited layer obtained from such growth mode is weakly attached to the substrate and is associated with a rough surface. The “Stransky-Krastanov” growth mode (island growth on top of predeposited monolayers) occurs when using additives providing moderate inhibition [15]. As a matter of fact, the additives preferentially adsorb on the defect sites thus forcing the metal ions to discharge in the atomic planes rather than steps and kinks. An initial later growth of the film is obtained forming a monolayer where, as the deposited layer builds up, island nuclei will form and grow. Finally, when applying a stronger inhibition, a layer-by-layer growth is obtained leading to smooth and fine grained deposits [15]. Depending on the type of growth of the electrodeposited film, different microstructures can be formed. A classification of the different microstructures commonly encountered was provided by Fisher [19] and then re-proposed by Winand [20]:

1. field-oriented isolated crystals type (FI);
2. basis-oriented reproduction type (BR);
3. twinning intermediate type (Z);
4. field-oriented texture type (FT);
5. unoriented dispersion type (UD).

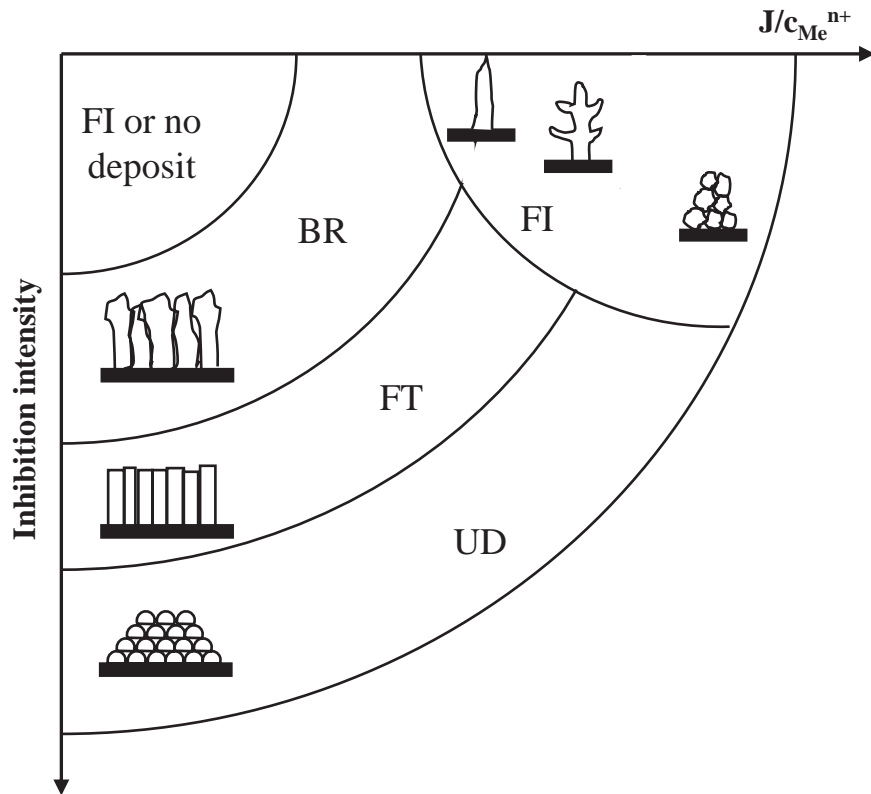


Figure 5: Diagram showing the different microstructures commonly found in electrodeposits as a function of the inhibition intensity and the ratio between current density and the concentration of the metal ions ( $j/C_{Me}^{Z+}$ ). Adapted from [20].

The FI type is occurring with low inhibition, and by increasing the current density unstable film structures will be formed, such as whiskers, dendrites and powder deposits [20]. The BR type is formed with moderate inhibition promoting an initial lateral growth of the film, which is then followed by the formation of larger crystals and by the possible degradation from BR type to FI type structure. The FT type is obtained at quite strong inhibition, leading to the formation of elongated crystals perpendicular to the substrate (columnar structure). The UD type is obtained at even higher inhibition, leading to the formation of a coherent deposit with randomly arranged fine grains. Finally, the twinning intermediate type (Z) is described by Fischer as a transitional microstructure from the BR to the FT type. A schematic diagram describing the different microstructure types as a function of the inhibition intensity and the ratio between the current density and the concentration of metal ions  $j/C_{Me}^{Z+}$  as proposed by Winand [20] is shown in Fig. 5. In this schematic drawing, the twinning intermediate microstructure (Z) is not included.

The peculiar microstructures incurred in electrodeposited coatings, together with the co-deposited impurities within the coatings, are the main reason why the physical, chemical and mechanical properties of electrodeposited metals and alloys usually differ from the properties

of the pure metallurgical samples [3]. The inclusion of impurities is often related to the presence of additives in the solution. Carbon is often found in coatings deposited using organic additives. The precipitation and co-deposition of hydroxide compounds is observed when the pH at the electrode/solution interface is sufficiently high to cause metal hydrolysis in the vicinity of the cathode [3]. In an electrochemical environment, the nucleation and growth process leading to microstructure development deviates strongly from the equilibrium conditions due to the large driving force for crystallization (i.e. current density or potential). Hence, the resulting microstructure is metastable, i.e. is out of equilibrium, and contains a high concentration of structural defects (i.e. grain boundaries, twin boundaries and dislocations) [3]. In addition, alloys produced by this method can show considerable extensions of the solid solubility range.

## 2.4 Nanocrystalline and amorphous electrodeposits

First studies on the electrodeposition of nanocrystalline materials were published in the late 1980s [21]. Since the first studies, electrodeposition of nanocrystalline materials has rapidly grown reaching commercial applications [4]. Electrodeposition can be considered as a grain boundary engineering process which allows to control the volume fractions of grain boundaries during the deposition of the material [5]. As mentioned in the previous chapter, the electrodeposition of materials typically occurs far from equilibrium conditions. The deposited material is then characterized with a large volume fraction of grain boundaries which is associated with small grain sizes. Figure 6 shows a schematic representation of the volume fraction of grain boundaries and total intercrystalline region in the grain size range from 2 nm to 1 mm, as calculated by Palumbo et al. [22]. The total intercrystalline volume fraction is calculated assuming a 14-sided tetrakaidecahedron as grain shape, and a grain boundary thickness ( $\Delta$ ) of 1 nm. As can be seen from the graph, when the grain size is reduced below 100 nm, both the grain boundary fraction and the intercrystalline volume fraction begin to account for a significant volume fraction of the material (50% at a few nm in grain size).

Several material properties are effected by the grain size refinement and the associated increased volume fraction of the intercrystalline region. Mechanical properties like the material hardness and the yield strength show a considerable increase with decreasing the grain size [5].

Electrodeposition can also be applied to deposit amorphous materials, i.e. glass-like materials with no long range ordering. Amorphous alloys are usually formed upon the co-deposition of non-metallic components (boron, phosphorous, sulfur, oxides and hydroxides) or refractory components, e.g. tungsten [3]. These components, when deposited in sufficiently high amount (i.e. at least 15 at.%), act as amorphizing additives and inhibit the crystallization process. As a matter of fact, the addition of these components leads to a drastic decrease in the diffusion rate of the elements in the system [3]. The amorphous structure influences to a large extent the properties of the materials. Amorphous materials are often very hard and can exhibit high corrosion resistance [23] due to the absence of dislocations and grain boundaries, respectively. In consideration to their enhanced properties, nanocrystalline and amorphous alloys are of great interest for protective coating applications. However, due to their peculiar structure, nanocrystalline and amorphous materials are in a metastable state, thus there is a strong driving force for grain growth and crystallization of stable phases with increasing the temperature. Hence, the thermal stability of these materials can be rather low.

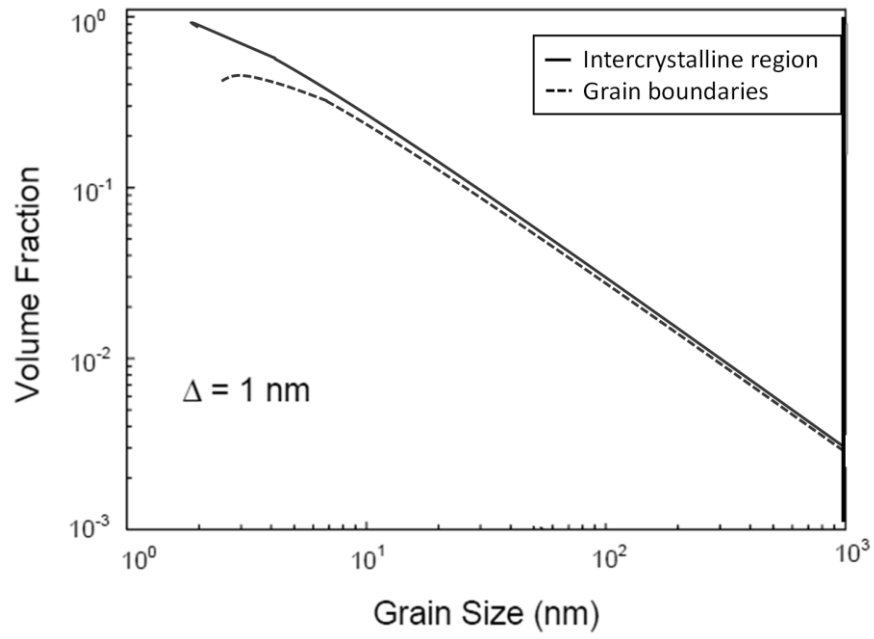


Figure 6: The effect of grain size on the volume fractions of intercrystalline regions and grain boundaries, assuming a grain boundary thickness,  $\Delta$ , of 1 nm. Adapted from [22].

### 3 Analyzed materials and deposition method

In this chapter the deposition method for the studied materials, i.e. pure tin (Sn) and FeW coatings, is presented together with some previous studies done on both materials.

#### 3.1 Previous studies on Fe-W electrodeposits

Electrodeposition of Fe-W coatings is studied since the 1940s [24,25]. The electrolytes used for the deposition of the alloy have changed over the years and still today the development of new electrolytes are required. Citrate baths with Fe(II) salts have been repeatedly investigated [26–28], also with the addition of ammonia to increase the solubility of the metal complexes [25,29]. The deposition from citrate-ammonia baths resulted in smooth Fe-W coatings with a silvery/grey appearance [30]. However, in order to reduce the environmental impact of the electrolytes, the use of ammonia has been progressively discouraged. Hence, ammonia-free baths started to be studied and applied for the deposition of Fe-W coatings [31,32]. A further development of the electrolytes involved the use of Fe(III) salts in order to avoid oxidation of Fe(II) species (i.e.  $\text{Fe}^{2+}$  dissolved ions will oxidize to  $\text{Fe}^{3+}$  ions) [33]. The use of ammonia in Fe(II)-Fe-W electrolytes was also intended to stabilize the bath by hindering the Fe(II) oxidation process, which still cannot be fully prevented [2]. However, the deposition from Fe(III) solutions is commonly characterized with rather low current efficiency and the obtained coatings have a lower W content as compared to the alloys deposited from Fe(II) electrolytes [25,30,34]. Remarkable improvements have been achieved from an environmentally friendly Fe(III)-based glycolate-citrate electrolyte recently developed. From this bath, by properly changing the deposition parameters (i.e. pH, temperature and current density), Fe-W coatings with tungsten content varying from few at.% to 25 at.% can be deposited with current efficiency up to 60-70% [35,36].

Generally, the structure of Fe-W alloys vary from nanocrystalline to amorphous with increasing the W content of the alloy [26]. A nanocrystalline solid solution is formed in Fe-W coatings deposited with relative low W content. The coatings retain the structure of the base metal, in this case bcc-iron, with an increased lattice parameter as compared to pure iron [26]. For Fe-W coatings with W content ranging from 11.5 to 20 at.% a mixed amorphous-crystalline structure was found [37]. Fully amorphous Fe-W coatings are usually obtained when deposited with a W content higher than 20 at.% [32,38].

For Fe-W coatings deposited with high W content, i.e. > 20 at.%, previous studies were mostly aimed to assess the material's as-deposited hardness [36,39], the material's thermal stability [38], or the influence of thermal treatments on the corrosion properties [32]. For lower W containing coatings, studies were mainly focused on assessing the magnetic properties of the material [36,40].

#### 3.2 Electrodeposition of Fe-W alloys

Fe-W coatings with 4, 16 and 24 at.% of W were deposited from a glycolate-citrate plating bath with the following composition: 1 M glycolic acid, 0.3 M citric acid, 0.1 M  $(\text{Fe})_2(\text{SO}_4)_3$  and 0.3 M  $\text{Na}_2\text{WO}_4$ . The deposition conditions are given in Table 1. The used deposition parameters were optimized and selected after studying their influence on the co-deposition of W with Fe [36]. The deposition of the Fe-W coatings was performed in a typical three-electrode cell. A pure copper sheet was used as the working electrode, platinized titanium was used as a counter

electrode, and saturated Ag/AgCl/KCl<sub>sat</sub> was used as reference electrode. The current efficiency, CE, was calculated based on Faraday's law. The calculation is described elsewhere [36]. The chemical composition of the three Fe-W coatings was measured by EDS analysis and is also presented in Table 1. The composition of the three alloys is presented as content of the metallic phase only, i.e. Fe and W, and also considering the O content as detected by EDS measurement on the sample surfaces. Figure 7 shows the elemental distribution profiles of the three Fe-W coatings, as measured from GD-OES analysis. GD-OES measurements were performed in order to get reliable compositional depth profiles (CDP) and to determine if impurities such as O and C are co-deposited with Fe and W. The results in Fig. 7 show that electrodeposited Fe-W coatings contain up to 80 at.% of O and 10 at.% of C at the top of the coatings. The amount of these elements decreases sharply within the first 0.5  $\mu\text{m}$ . O is distributed along the entire film thickness only in the coating with low W content, see Fig. 7a. In all three analysed coatings, the carbon content is lower than at the surface, i.e.  $\sim$ 1-2 at.% for the samples with 4 at.% and 16 at.% of W, and  $\sim$ 0.3 at.% for the sample with 24 at.% of W, respectively.

*Table 1: Operating conditions and EDS chemical composition of as-deposited Fe-W coatings.*

Sample	T, °C	pH	j, mA cm <sup>-2</sup>	CE, %	-E, V	Composition (at.%)				
						Fe	W	O	Fe	W
1	20	6.5	15	24	1.25	80	4	16	96	4
2	65	5.0	15	50	1.04	59	10	31	84	16
3	65	6.5	15	72	1.08	64	20	17	76	24

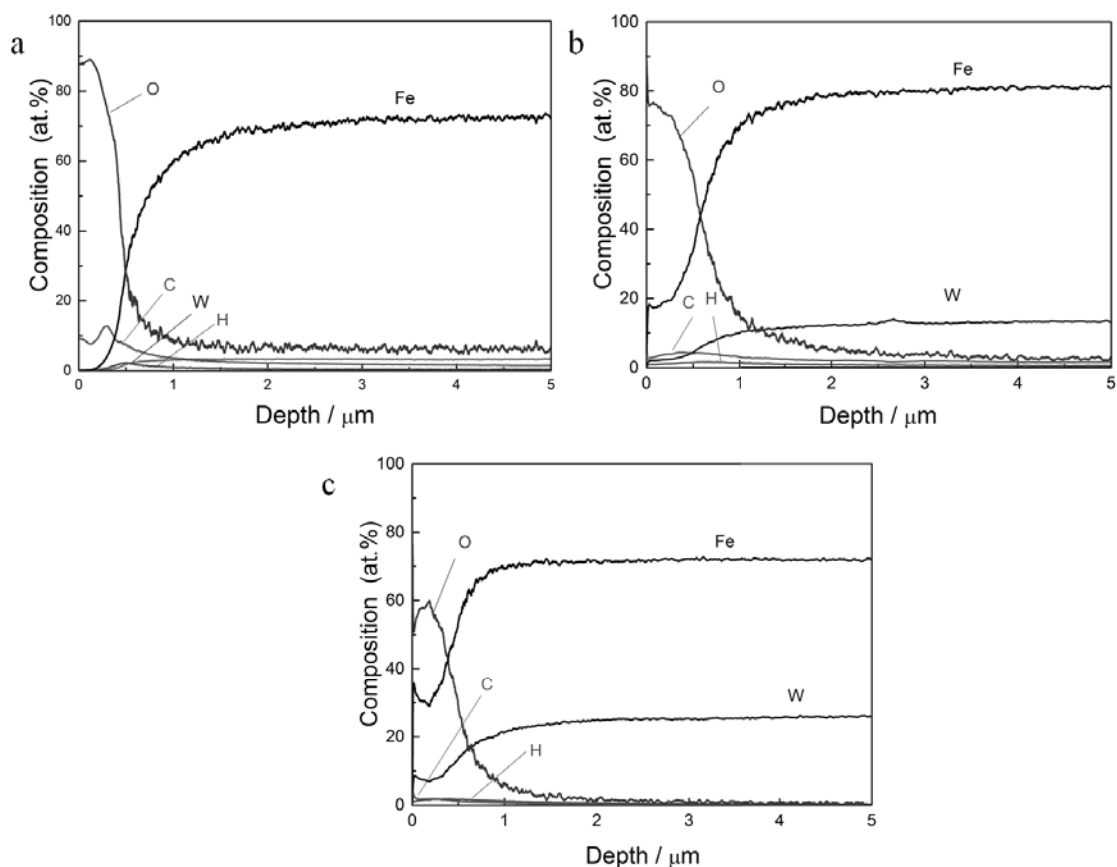


Figure 7: Compositional depth profiles measured by GD-OES of Fe-W samples with different composition: 4 at.% of W (a), 16 at.% of W (b) and 24 at.% of W (c).

### 3.3 Previous studies on electrodeposited Sn

Tin electrodeposition can be performed from both alkaline and acidic electrolytes from the reduction of either Sn(II) or Sn(IV) species [41]. In acidic solutions both Sn(II) and Sn(IV) are stable, thus Sn(II) can be easily oxidized to Sn(IV) through atmospheric oxidation. The consequences are losses in the deposition rate of the used electrolyte [15]. However, acidic electrolytes used for tin plating generally contain antioxidant additives to minimize Sn(IV) formation. The additive inhibits the oxidation process by either forming stable complexes with Sn(II) ions, or by reducing the oxygen solubility in the solution [15]. Acidic solutions commonly used for tin deposition are sulfuric [42], phenosulfonic [43], methanesulfonic [44–47] or chloridic based electrolytes [48,49]. These electrolytes are operated at room temperatures and by using a soluble anode. Alkaline electrolytes are based on sodium or potassium stannate, with simple compositions and can operate without the use of additives [15]. However, alkaline electrolytes are less often used as compared to the acidic electrolytes for tin electrodeposition. This is due to some drawbacks that are incurred when operating with an alkaline electrolyte. Due to the stannate form of the tin, i.e. Sn(IV), in the alkaline electrolytes the electrochemical equivalent is only half of the one in acidic baths. High cathodic current densities can be achieved in alkaline baths only when they are operated at high temperatures ( $> 60\text{ }^{\circ}\text{C}$ ). Furthermore, to maintain reasonable current efficiency the alkaline concentration of the baths has to be kept under control in order to avoid any hydrolysis of the Sn(IV) ions [15].

Tin can be present in two allotropic forms:  $\beta$ -Sn with a body-centered tetragonal crystal structure and  $\alpha$ -Sn with a diamond crystal structure [15]. The  $\alpha$ -Sn structure is not commonly found. As a matter of fact, the allotropic transformation from  $\beta$ -Sn to  $\alpha$ -Sn occurs at 13 °C and is extremely slow [15]. Tin metal is silver-white, soft, non-toxic, and has excellent corrosion resistance [50]. Thanks to its non-toxicity and corrosion resistance, tin can be used in an unalloyed form for contact with food (i.e. tin can for food storage). Furthermore, thanks to its solderability, it is also used in the electronics industry [44].

### 3.4 Electrodeposition of Sn

For the electrodeposition of Sn coatings a chloride electrolyte and a methane sulfonic acid (MSA) electrolyte were prepared. The composition of the two baths is provided in Table 2. The coatings were deposited on 1 x 1 cm<sup>2</sup> flat brass substrates using direct current for 15 minutes in an IPS PGU 20V-2A-E potentiostat/galvanostat. The electrolyte was kept static or it was agitated with 250 rpm using a magnetic stirrer during the deposition. The chloride electrolyte had a pH of about 5 and was operated at a temperature of 60°C. The applied current density was -0.5 A/dm<sup>2</sup>. The MSA electrolyte was operated at room temperature, had a pH of about 0.5 and the current density used was -1.5 A/dm<sup>2</sup>. For the purpose of depositing homogenous and compact layers alkoxylated  $\beta$ -naphthol (ABN) additive was added to both electrolytes in different concentrations: 0, 0.78, 1.56 and 3.12 mg/l.

Table 2: Composition of the chloride based and MSA electrolytes.

	Chloride (g/l)	MSA (g/l)
SnCl <sub>2</sub> . 2 H <sub>2</sub> O	25	-
Na <sub>3</sub> C <sub>6</sub> H <sub>5</sub> O <sub>7</sub> ( <i>Sigma Aldrich</i> )	80	100
KNaC <sub>4</sub> H <sub>4</sub> O <sub>6</sub> . 6H <sub>2</sub> O ( <i>Carl Roth</i> )	25	-
(NH <sub>4</sub> ) <sub>2</sub> SO <sub>4</sub> ( <i>Sigma Aldrich</i> )	60	-
MSA (70%) ( <i>Carl Roth</i> )	-	157 ml/l
SnMSA (300 g/l Sn <sup>2+</sup> ) ( <i>Atotech</i> )	-	166 ml/l

## 4 Characterization techniques

In this chapter the different techniques used to characterize the electrodeposited materials are introduced.

### 4.1 Imaging techniques

To characterize the different electrodeposited materials various imaging techniques were used in this work, i.e. Scanning Electron Microscopy, Electron Back Scatter Diffraction, and Transmission Electron Microscopy.

#### 4.1.1 Scanning Electron Microscopy (SEM)

Scanning electron microscopes are one of the most versatile instruments to analyze microstructural characteristics of solid materials. One of the main reasons is the high resolution that can be achieved: using electrons as imaging source allows to overcome the limited image resolution of light optical microscopes that is imposed by the wavelength of visible light.

In SEMs, the electrons are generated in an electron gun (the source can be of different type, i.e. tungsten filament, LaB<sub>6</sub> or field emission guns) and afterwards, they are focused onto the surface of the sample by means of electric and magnetic lenses. When the focused electron beam scans across the sample surface, the interactions between the electrons and the atoms in the sample lead to the emission of different types of signals. These radiations are generated from the interactions at different depths of the so-called three-dimensional interaction volume [51]. The interaction volume is in the range of micrometers and its depth can vary depending on factors such as the atomic number of the material analyzed, the accelerating voltage of the electron beam and its angle of incidence. Figure 8 shows a schematic representation of interaction volume and of the signals generated.

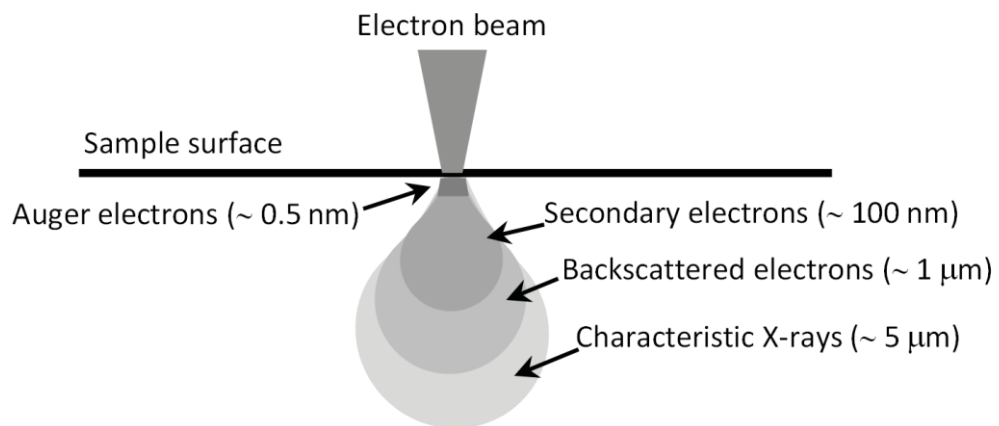


Figure 8: Schematic representation of the electron beam-sample interaction volume and the signals generated in the SEM.

Secondary electrons (SE) and backscattered electrons (BSE) are the signals commonly used for imaging. SE are the specimen electrons emitted by the inelastic scattering of the electron beam. Such electrons escape from depths in the order of 100 nm due to their low kinetic energy, <50 eV, and are used for imaging surface topography. BSEs are instead generated from elastic scattering of the incident electron beam. These electrons are highly energetic and thus they can

originate from a depth of around 1  $\mu\text{m}$ . The elastic scattering is strongly dependent on the atomic number of the target atom, thus BSE can be used to obtain chemical contrast imaging: atoms of heavy elements backscatter more electrons and will appear brighter. The electron beam-surface interaction causes the emission of an inner shell electron, thus leaving the atom in an excited state. The inner vacant site is then filled by an outer shell electron, which leads to the relaxation of the atom to its ground state. The excess energy related to this process is emitted in the form of X-rays. The energy of the X-rays is defined by the difference between the energy levels of the electrons involved in the process, and therefore it is characteristic of the electronic structure of the analyzed material. These X-ray signals can be collected and used to perform chemical composition analysis. When performing such analysis, it is however important to consider the interaction volume of the X-rays. In fact, the interaction volume of X-rays can be up to 5  $\mu\text{m}$  and this can limit the reliability of the measurements when analyzing features with sizes in the micrometer scale or below [51].

#### **4.1.2 Electron Back Scatter Diffraction (EBSD)**

EBSD is a powerful characterization technique available in SEM which provides microstructural and crystallographic information of crystalline materials. This technique can be used to reveal grain size and grain shape, grain boundary character distribution, grain orientation (texture), as well as phase discrimination [52] with or without the use of EDS. For EBSD analysis, the sample surface must be polished and highly tilted (i.e.  $70^\circ$ ). EBSD analysis can be performed by spot analysis or by scanning the electron beam with a chosen step size over a defined area of the investigated specimen. The interaction of the electron beam with the crystalline specimen generates diffraction cones which are then detected by a phosphor screen placed in the vicinity, as shown schematically in Fig. 9. The diffracting cones form in the phosphor screen a regular arrangement of parallel bright bands, known as Kikuchi bands, on a continuous background [53]. The generated Kikuchi diffraction pattern is characteristic of the crystal structure and the local orientation at the point of interest. Hence, with a priori information about the expected phases in the material, the computer software indexes the acquired EBSD patterns by comparison with crystallographic data of the expected phase. From the EBSD patterns, information about the orientation and the phase are collected. If the indexing is not possible, i.e. due to poor EBSD pattern quality, overlapping patterns from adjacent grains, or due to the presence of an undefined phase, the obtained pixel is recorded as a “zero-solution” [52]. Performing EBSD analysis over a defined area of the specimen allows to determine orientation maps or phase maps. The obtained maps are then used to reveal information regarding e.g. the grain size and orientation of the analyzed sample.

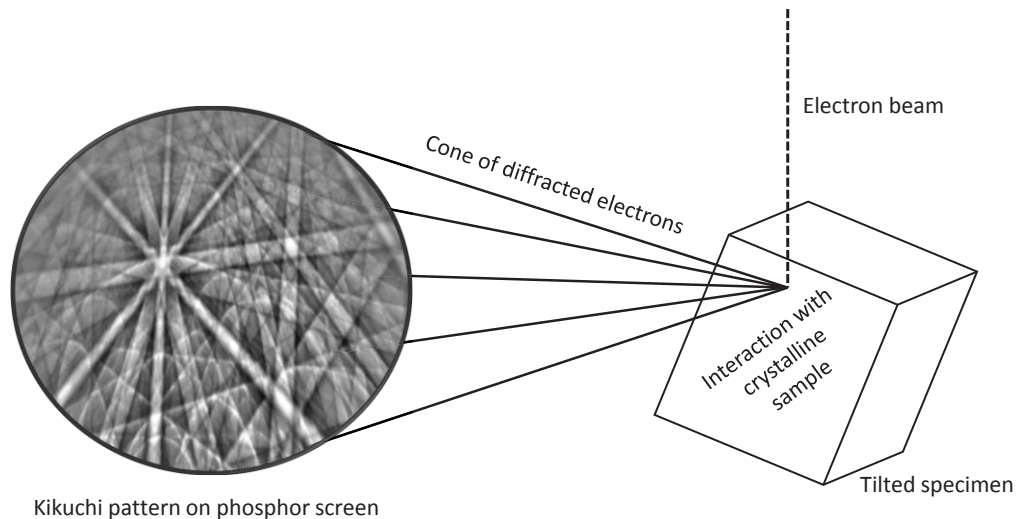


*Figure 9: Schematic representation of the electron interaction with a crystalline material and the EBSD pattern generated. Adapted from [52].*

### 4.1.3 Transmission Electron Microscopy (TEM)

A Transmission Electron Microscopy uses electrons as imaging source, as in the case of an SEM. However, when working with a TEM the applied accelerating voltage is much higher, i.e. ranging from 100 kV to 1.2 MV, which allows to reach high resolution imaging down to fractions of nanometers. The working principle of a TEM consists of the irradiation of a thin sample (less than 100 nm in thickness) with a high-energy electron beam. Thanks to the high accelerating voltage applied and to the small sample thickness, most of the electrons are transmitted through the sample, while some of the incident electrons interact with the atoms of the sample and are diffracted. This allows two different imaging modes: bright field imaging by use of the transmitted electrons, and dark field imaging making use of the diffracted electrons. The imaging mode can be selected to be either a bright field or dark field image by adjusting the objective aperture. Working with TEM allows also to alternate between imaging mode and diffraction mode by changing the strength of the intermediate lens/diffraction lens. The diffraction mode is used to obtain information on the crystal structure of the sample and on its orientation, which is done through the study of the diffraction patterns of the analyzed sample. On Fig. 10 is shown a schematic representation of the of the diffraction pattern obtained when analyzing a single crystal, a polycrystalline and an amorphous material.

The TEM used in this work is a Zeiss EM 912 Omega which is equipped with a LaB<sub>6</sub> electron gun and operating at an acceleration voltage of 120 kV. Both image and diffraction mode were used to characterize the electrodeposited Fe-W sample. The specimen was a substrate-free sheet with a thickness of around 15  $\mu\text{m}$ . Discs with a diameter of 3 mm were punched from the sheet and then thinned by ion milling on both sides with an angle of incidence of 4<sup>0</sup>.

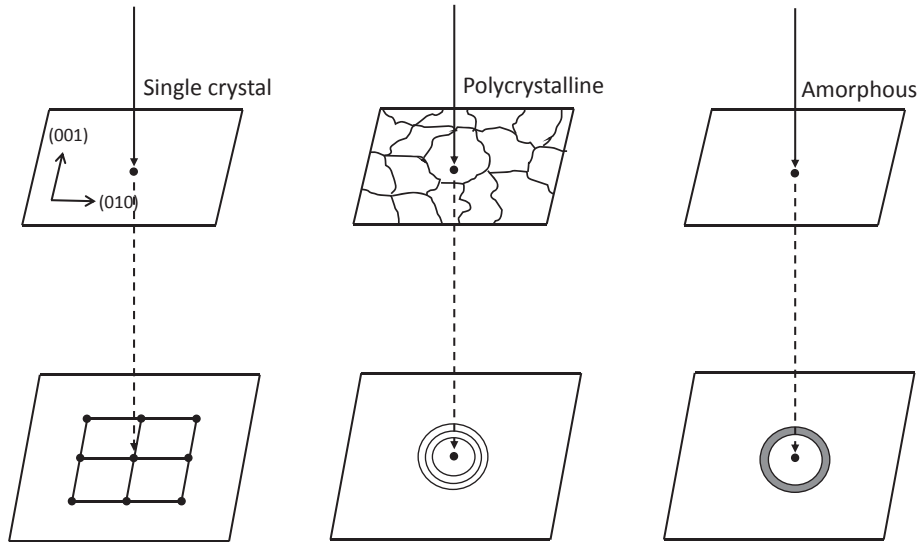


Figure 10: Schematic representation of different diffraction pattern obtained from a single crystal, polycrystalline and amorphous material, adapted from [54].

## 4.2 Non-imaging techniques

The electrodeposited coatings were also characterized by means of X-ray diffraction analysis, glow discharge optical emission spectroscopy, and nanohardness measurements.

### 4.2.1 X-ray diffraction (XRD)

X-ray diffraction is a common technique for phase identification analysis. Its working principle is based on X-ray diffraction: a monochromatic X-ray beam irradiates the sample while a rotating XRD detector measures the intensity of the diffracted X-rays as a function of  $2\theta$ . The phase identification is performed by converting the diffraction angle  $\theta$  into interplanar distances, as described by Bragg's law:

$$n\lambda = 2d \sin \theta$$

Where  $n$  stands for the diffraction order,  $\lambda$  for the wavelength of the X-ray beam,  $d$  for the interplanar distance, and  $\theta$  for the diffraction angle. Moreover, the sets of diffraction planes can also be compared with those from a powder standard database. A standard powder is characterized by a random texture. Hence, comparing the measured intensities of the sets of diffraction planes with the intensities from a standard powder can provide an indication of the possible texture of the sample.

In this work, the instrument used for phase identification on the Fe-W coatings was a Rigaku MiniFlex II diffractometer with Cu  $K\alpha$  radiation ( $\lambda=1.54183 \text{ \AA}$ ) operated at 30 kV and 30 mA. The texture analysis on electrodeposited Sn was performed using a Bruker AXS D8 advance diffractometer with Cr  $K\alpha$  radiation ( $\lambda=2.0821 \text{ \AA}$ ) operated at 35 kV using a grazing incidence geometry with the angle of incidence set to  $3^\circ$ . In this case the grazing incidence geometry was used to avoid the detection of the substrate peaks. As a matter of fact, the grazing incidence configuration allowed to reduce the information depth to  $\sim 250 \text{ nm}$  from the surface of the Sn sample.

#### **4.2.2 Glow discharge optical emission spectroscopy (GD-OES)**

Glow Discharge Optical Emission Spectroscopy (GD-OES) is a destructive spectroscopic technique for qualitative and quantitative chemical analysis. The technique is commonly used to obtain compositional depth profiles (CPD) of relative thick coatings (up to hundreds of microns) with high sensitivity for both heavy as well as light elements such as O, C and H.

The GD-OES measurement chamber is filled with Ar gas at low pressure and a high direct voltage is applied between the anode and the sample to be analyzed (cathode). The electrons released from the sample surface trigger the formation of high energy Ar cations leading to a sputtering process which progressively removes atoms from the sample surface. The ejected atoms are excited by the interaction with the high energy electrons present in the plasma and, on returning to their ground state, emit photons with a characteristic wavelength which are collected and analyzed. The intensity of the recorded signal is proportional to the concentration of the corresponding element in the plasma, providing then quantitative information of the material composition.

In this work the instrument used was a GDA750HR (Spectrumba) with 2.5 mm source in DC mode. The discharge was operated in a high-purity Ar atmosphere and constant current (10 mA)/constant voltage (700 V) control mode.

#### **4.2.3 Nanohardness measurements**

Hardness measurements on the as-plated and annealed coatings were performed using a NHT<sup>2</sup> Nanoindentation Tester from Anton-Paar which was equipped with a Berkovich pyramidal-shaped diamond tip under-load control mode. A load of 10 mN was applied with a loading segment of 30 seconds, followed by a load holding segment of 10 seconds, and by an unloading segment of 30 seconds. The hardness is reported as an average value of fifteen measurements performed in the middle of the cross-section of each sample. For the nanoindentation measurements the cross-sections were polished down to a 1  $\mu\text{m}$  surface finish. In Fig. 11 is shown a load vs. displacement curve measured from the as-deposited Fe-W sample with 24 at. % of W. SEM images of the nanoindentations performed on the cross-section of the three as-deposited Fe-W samples are also included in Fig. 11. The values of the hardness are extracted from the load-displacement curves according to the method of Oliver and Pharr [55].

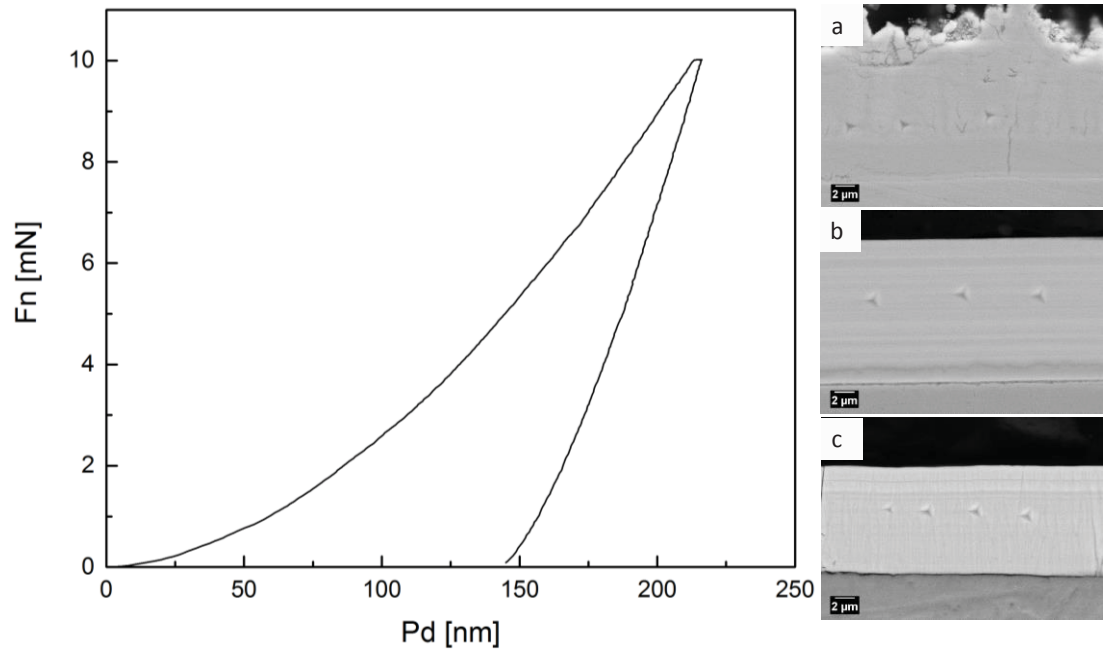


*Figure 11: Load (Fn) vs. displacement (Pd) curve measured for the as-deposited Fe-W coating with 24 at.% of W. SEM images showing the indent imprint on the cross-section of the Fe-W coating with 4 at.% (a), 16 at.% (b) and 24 at.% (c) of W.*

## 5 Summary of results and discussions

The results presented in the three attached papers are here shortly discussed. Depending on the type of material analyzed, i.e. Sn and Fe-W coatings, the results are divided in different subchapters. The three included papers are listed below. It is also specified in which subchapter the results are discussed:

- Paper 1 – “In-depth characterization of as-deposited and annealed Fe-W coatings electrodeposited from glycolate-citrate plating bath” is covered in subchapter 5.1.1
- Paper 2 - “The effect of heat treatment on the structure and on the hardness of Fe-W alloys electrodeposited from a glycolate-citrate plating bath” is covered in subchapter 5.1.2
- Paper 3 - “Alkoxyated  $\beta$ -naphthol as an additive for tin plating from chloride and methane sulfonic acid electrolytes” is covered in subchapter 5.2.1 and 5.2.2.

### 5.1 Characterization of electrodeposited Fe-W alloys

#### 5.1.1 Interdependences between the composition, the structure and the thermal stability of Fe-W coatings

Generally, the structure of W alloys varies from nanocrystalline to amorphous with increasing the W content in the alloy [26]. Thus, Fe-W alloys can be deposited with an amorphous [27] or nanocrystalline structure by proper tuning the composition of the alloy [39]. As a confirmation, the XRD results acquired from the as-plated Fe-W samples with 4, 16 and 24 at.% of W show how the crystallographic structure of the Fe-W coatings changes with increasing W content: a nanocrystalline structure is found for the 4 at.% W sample, a mixed nanocrystalline-amorphous structure for the sample with 16 at.% W, and a homogenous amorphous nature for the 24 at.% W sample, see Fig. 12. In the XRD profile of the sample with 16 at. % of W a small crystalline peak appears at the top of the amorphous shoulder which indicates the presence of a certain degree of crystallinity. To confirm the fully amorphous structure of the sample with 24 at.% of W, TEM analyses were performed. The TEM image in Fig 12b shows diffuse diffraction patterns, typical for an amorphous material (see also Fig. 10 in paragraph 4.1.3).

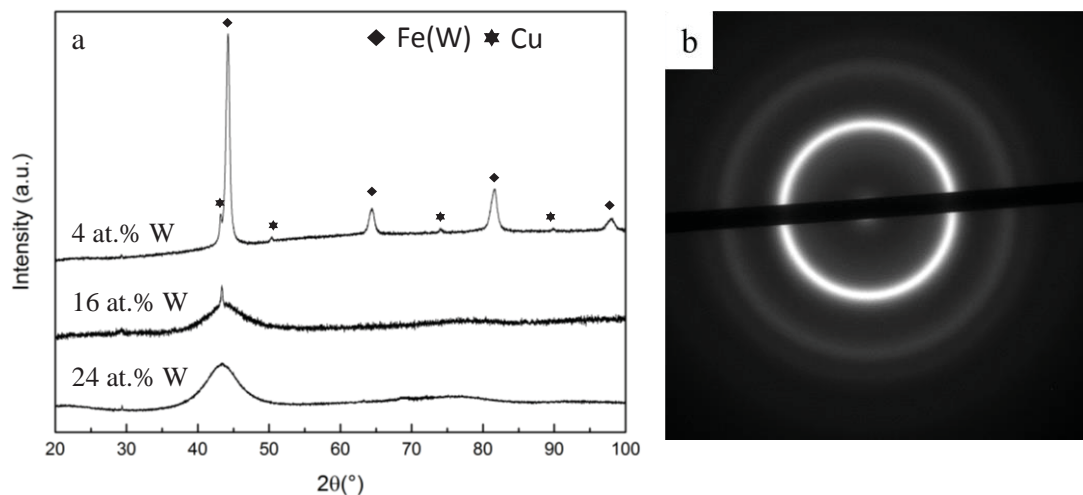


Figure 12: X-ray diffraction profiles of the as-deposited Fe-W samples (a) and TEM image of the selected area diffraction pattern of the sample with 24 at.% of W.

However, the tungsten content is not the only factor determining the structure and thus the properties of the alloy. As previously stated (see chapter 2.3), during the electrodeposition process various non-metallic elements (e.g. oxygen and carbon) can be co-deposited within the alloy and influence the microstructure development during the thermal treatment. GD-OES tests performed on the three Fe-W alloys allowed to get reliable composition depth profiles and to determine the presence of co-deposited impurities (see in chapter 3.2).

Vacuum annealing tests were performed on three samples to study the thermal stability of the Fe-W coatings and the structural changes occurring at each analyzed temperature. As shown by the XRD profiles in Fig. 13, the thermal stability of Fe-W alloys increases with the W content. The Fe-W sample with 24 at.% W retains the amorphous structure up to 600 °C, where a partially crystallized  $\alpha$ -Fe structure was observed. After annealing at 800 °C, the sample is still not fully crystalline (~30% of retained amorphous phase). The higher thermal stability can be associated to the lower rate of elemental diffusion obtained when adding a higher melting point element in the alloy, like in the case of W addition [56]. The phase transformation triggered by the annealing tests led to the formation of the following crystalline phases:  $\alpha$ -Fe,  $\text{Fe}_2\text{W}$ ,  $\text{Fe}_3\text{W}_3\text{C}$ ,  $\text{Fe}_6\text{W}_6\text{C}$ , and  $\text{FeWO}_4$ . The  $\alpha$ -Fe and  $\text{Fe}_2\text{W}$  intermetallic phase are both expected to be stable phases according to the binary Fe-W phase diagram [57,58]. The oxide and the carbide phases are instead formed due to the observed co-deposition of carbon and oxygen impurities while depositing the Fe-W coatings.

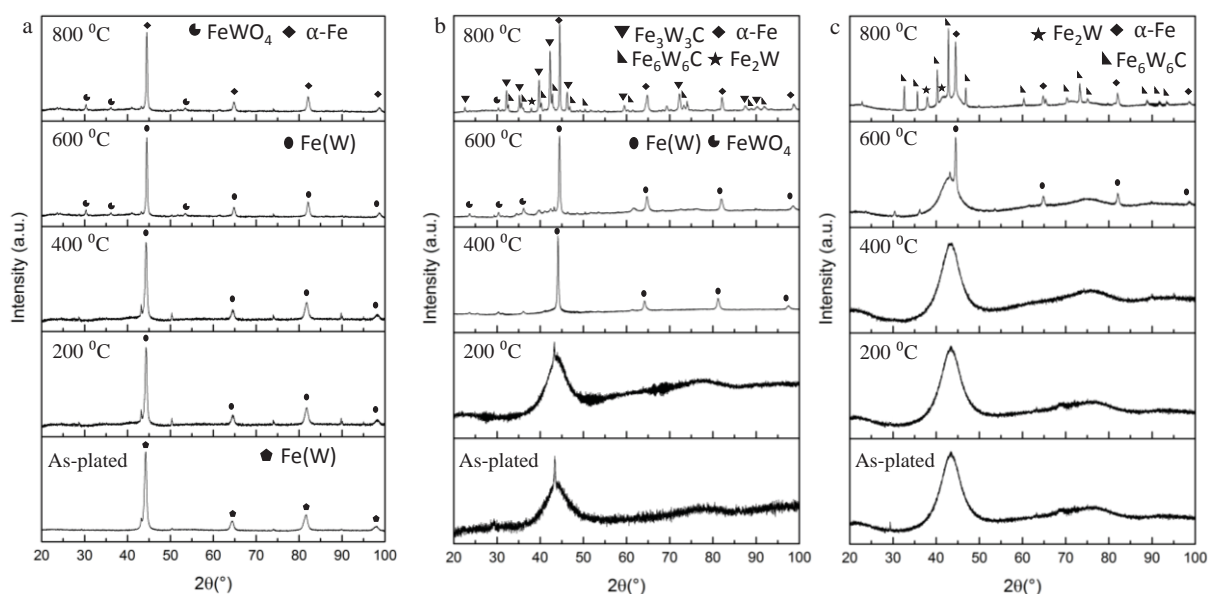


Figure 13: X-ray diffraction patterns for Fe-W alloys with (a) 4 at.% of W, (b) 16 at.% of W, and (c) 24 at.% of W annealed at different temperatures.

### 5.1.2 Heat treatment effects on the hardness and on the microstructure of Fe-W coatings

Previous studies on W alloys showed that proper thermal treatment can improve the hardness of the electrodeposited coatings due to the precipitation of fine crystallites [59,60]. The results obtained in this study show an evident increase of the as-deposited hardness, in particular for the samples with 16 and 24 at.% of W. As shown in Fig. 14, for both coatings the hardness increases up to 600 °C, where a maximum value of 16.5 GPa is found for the Fe-W alloy with 24at.% W. After annealing at 800 °C, substantial decrease in hardness occurred due to the

increase in grain size of the formed crystalline phases. The strengthening effect of the annealing treatments is less pronounced for the sample with 4 at.% of W. Only a slight increase of the hardness was seen up to 400 °C followed by a constant decrease at 600 °C and at 800 °C. Regarding the as-deposited hardness of Fe-W coatings it was found by previous studies [36] an increase in the hardness by increasing the W content in the coatings. In this study the same trend is not observed, see Fig. 14. As a matter of fact, the sample with 4 at.% of W shows surprisingly high hardness, i.e. ~10 GPa. However, such a high value could be explained by the presence of oxygen rich areas observed in the cross-section of the sample, see Fig. 2 in paper 2. This high oxygen content could lead to the formation of nanoscale oxides which, distributed along the sample grain boundaries, are reported to increase the measured hardness [59,61].

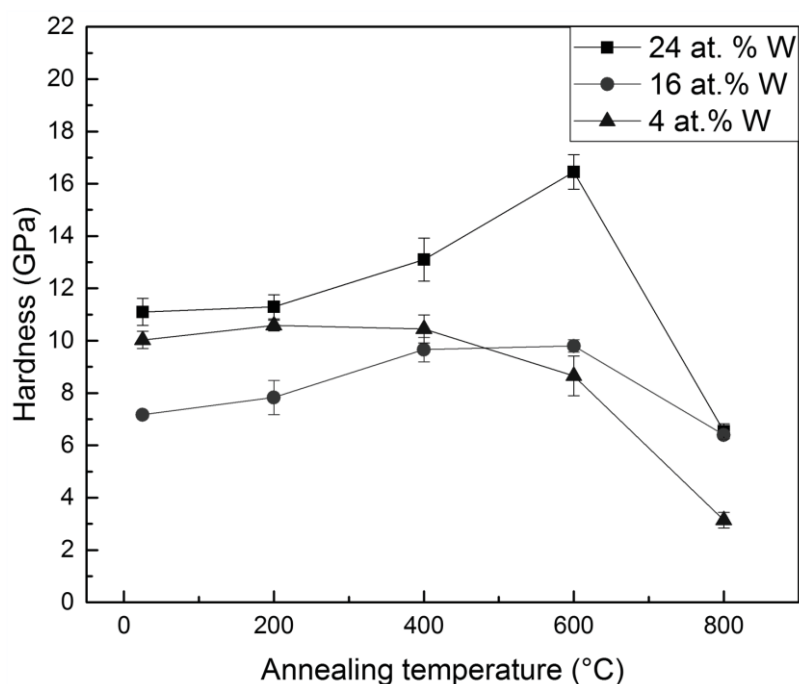


Figure 14: Hardness of the Fe-W coatings with 4 at.%, 16 at.% and 24 at.% of W are plotted as a function of the annealing temperature for 1 hour heat treatment.

The EBSD analysis performed on the cross-section of the samples annealed at 800 °C helped in understanding the microstructure development upon annealing and the distribution of the crystalline phases across the sample. In Fig. 15 are shown the back scattered electron images of the cross-section of the samples with 16 at.% and 24 at.% of W after annealing at 800 °C for 1 and 12 hours, Fig. 15a-b and Fig. 15c-d respectively. The red dashed box in the SEM images defines the area where the EBSD phase map was acquired. The phase maps are shown next to each back scattered electron image. For the sample with 16 at.% of W annealed at 800 °C for 1 hour the bright grains horizontally aligned in the cross-section are indexed as the carbide phase  $\text{Fe}_6\text{W}_6\text{C}$ . This is evident by looking at the line of carbides situated approximately 2  $\mu\text{m}$  from the substrate in Fig 15a. This area is highlighted in the back scattered electron image and in the corresponding phase map. In the sample with 24 at.% of W, the carbides appear to be distributed mostly along the substrate-coating interface and in proximity of the surface of the coating, see Fig 15c. What also appears from the map acquired from the 24 at.% of W is the large fraction of zero solutions, (presented in white in the phase map). Such high fraction of zero solutions

can be inferred to the nanocrystalline/amorphous nature of the sample which is preserved after the heat treatment and thus not possible to be indexed by EBSD technique. Bright grains are also visible for the sample with 16 at.% of W annealed at 800 °C for 12 hours, see Fig. 15b, and they are indexed as  $\text{Fe}_2\text{W}$  grains. Similarly, in the sample with 24 at.% of W the larger grains visible at the substrate-coating interface, where the  $\text{Fe}_6\text{W}_6\text{C}$  carbides were previously located, are indexed as  $\text{Fe}_2\text{W}$  after 12 hours annealing, see Fig 15d. These results indicate that longer annealing times result in the crystallization of stable phases as expected from the Fe-W binary phase diagram [57,58], which is observed with the dissolution of the carbides phases and the crystallization of the  $\text{Fe}_2\text{W}$  phase.

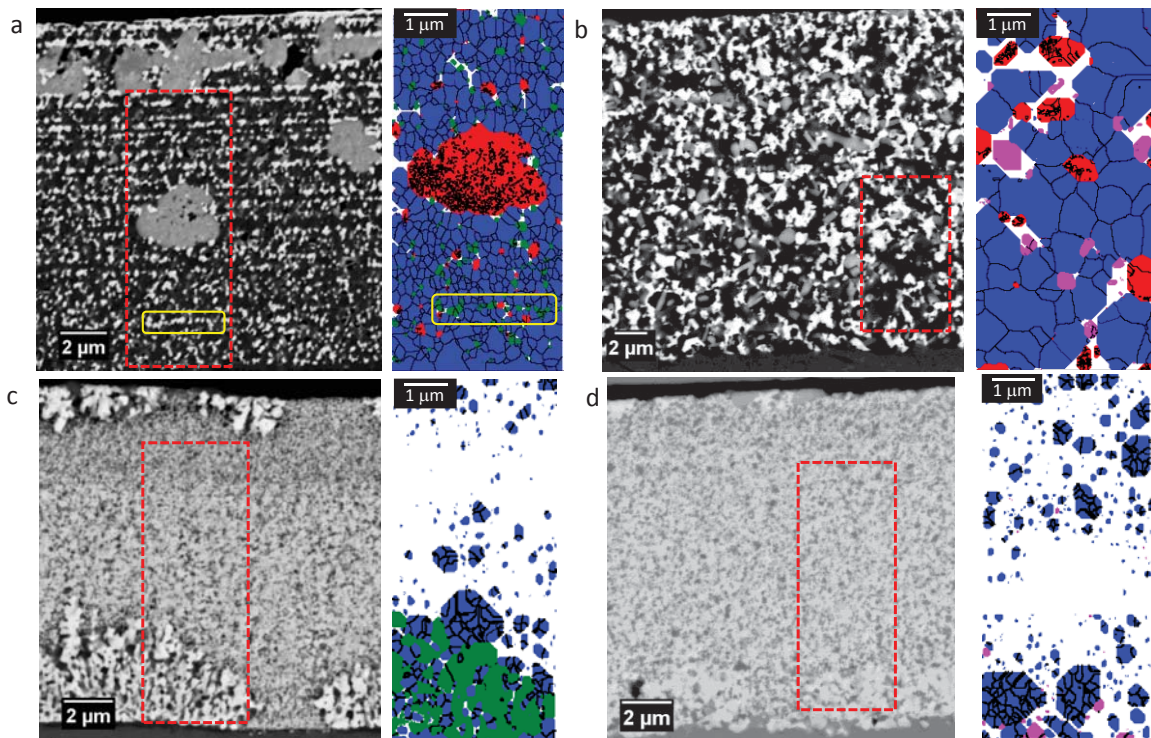


Figure 15: BSE image and phase map of the cross-section of the 16 at.% W sample annealed at 800 °C for 1 hour (a) and 12 hours (b). BSE image and phase map of the cross-section of the 24 at.% W sample annealed at 800 °C for 1 hour (c) and 12 hours (d); the EBSD phase maps are acquired from the red dashed box highlighted in each sample cross-section. Colour code: blue grains belongs to  $\alpha\text{-Fe}$  phase, the red grains to the  $\text{FeWO}_4$  phase, the green grains to the  $\text{Fe}_6\text{W}_6\text{C}$  phase, and the violet grains to the  $\text{Fe}_2\text{W}$  phase.

The EBSD results are also confirmed by XRD analysis performed on the 16 and 24 at.% W samples after annealing at 800 °C for 6 and 12 hours, see Fig 16. For the sample with 16 at.% of W. the carbide dissolution is more gradual. After 6 hours annealing at 800 °C the  $\text{Fe}_6\text{W}_6\text{C}$  peaks are still present in the XRD spectra. Only after annealing for 12 hours both carbides phases are strongly reduced, while the  $\text{Fe}_2\text{W}$  phase becomes more prominent, Fig 16a. For the sample with 24 at.% W after 6 hours heat-treatment most of the XRD peaks of the  $\text{Fe}_6\text{W}_6\text{C}$  phase are absent or strongly reduced, Fig 16b. Furthermore, a partial broad amorphous shoulder is still observed in the XRD diffractogram acquired after the 12 hours annealing. The retained

nanocrystalline/amorphous structure can explain the large fraction of zero solutions found also in the EBSD phase map acquired after 12 hours annealing, see Fig 15c.

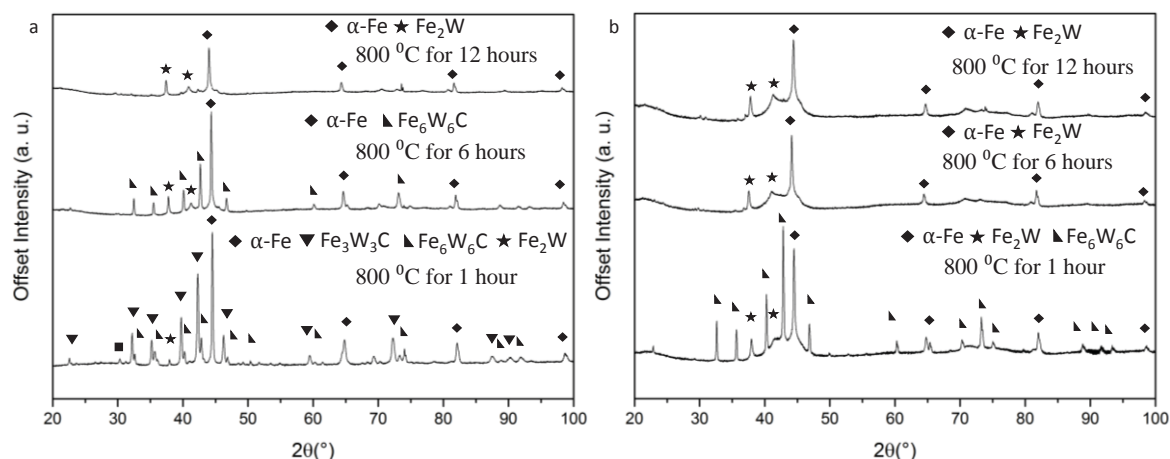


Figure 16: X-ray diffraction pattern evolution with increasing the annealing time (i.e. 1 hour, 6 hours and 12 hours) at 800 °C for the sample with 16 at.% of W (a), and for the sample with 24 at.% of W (b), respectively.

## 5.2 Characterization of electrodeposited Sn

### 5.2.1 Alkoxyated β-naphthol additive effects on the deposition of Sn

To investigate the influence of ABN in the chloride and MSA electrolytes, polarization and Tafel measurements were performed using an IPS PGU 20V-2A-E potentiostat. Fig. 17 shows the polarization curves of tin from both the chloride and MSA electrolytes for various ABN concentrations. In the measurements from the chloride electrolyte provided in Fig. 17a, with increasing the concentration of ABN is observed a decrease in the cathodic current density and the suppression of H<sub>2</sub> evolution. This behavior indicates that ABN molecules adsorb onto the cathode surface and hinder the cathodic reaction of metal deposition. In the measurements from the MSA electrolyte, Fig. 17b, with the addition of ABN the cathodic current is not suppressed as it happens in the chloride based electrolyte. A limiting current density plateau was found only in the case of a static electrode at ca. -670 mV (see Figure 6b in paper 3).

The different inhibition strength of ABN in the two electrolytes was also confirmed by the results from the Tafel measurements reported in Table 3. In the chloride electrolyte ABN acts as a highly effective inhibitor. At the concentration of 0.78 mg/l of ABN the exchange current density ( $J_0$ ) is almost one order of magnitude lower than in the case when no ABN additive is present. In the MSA electrolyte, adding ABN also reduces the exchange current density. However, in comparison to the chloride electrolyte, a higher ABN concentration is needed.

This results indicate that the ABN acts as an inhibitor in both chloride-based and MSA electrolyte, but in the case of MSA electrolyte higher ABN concentrations are needed.

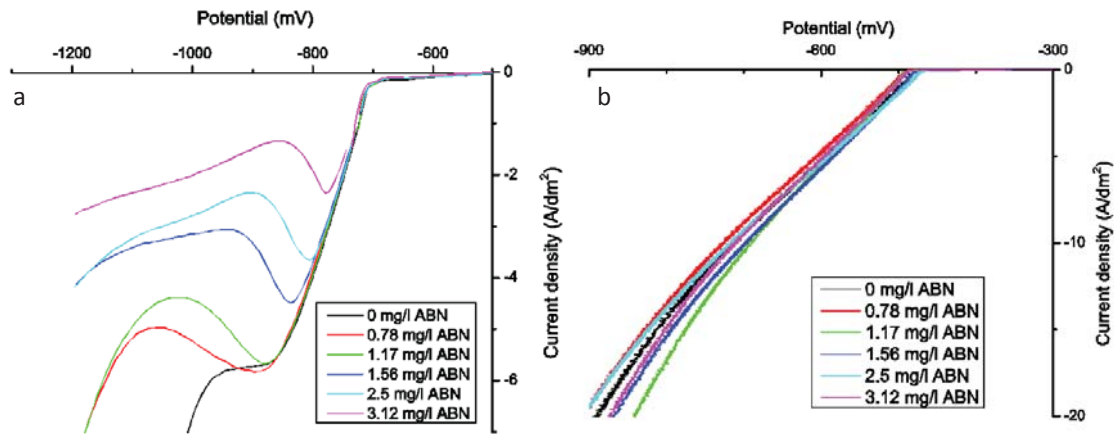


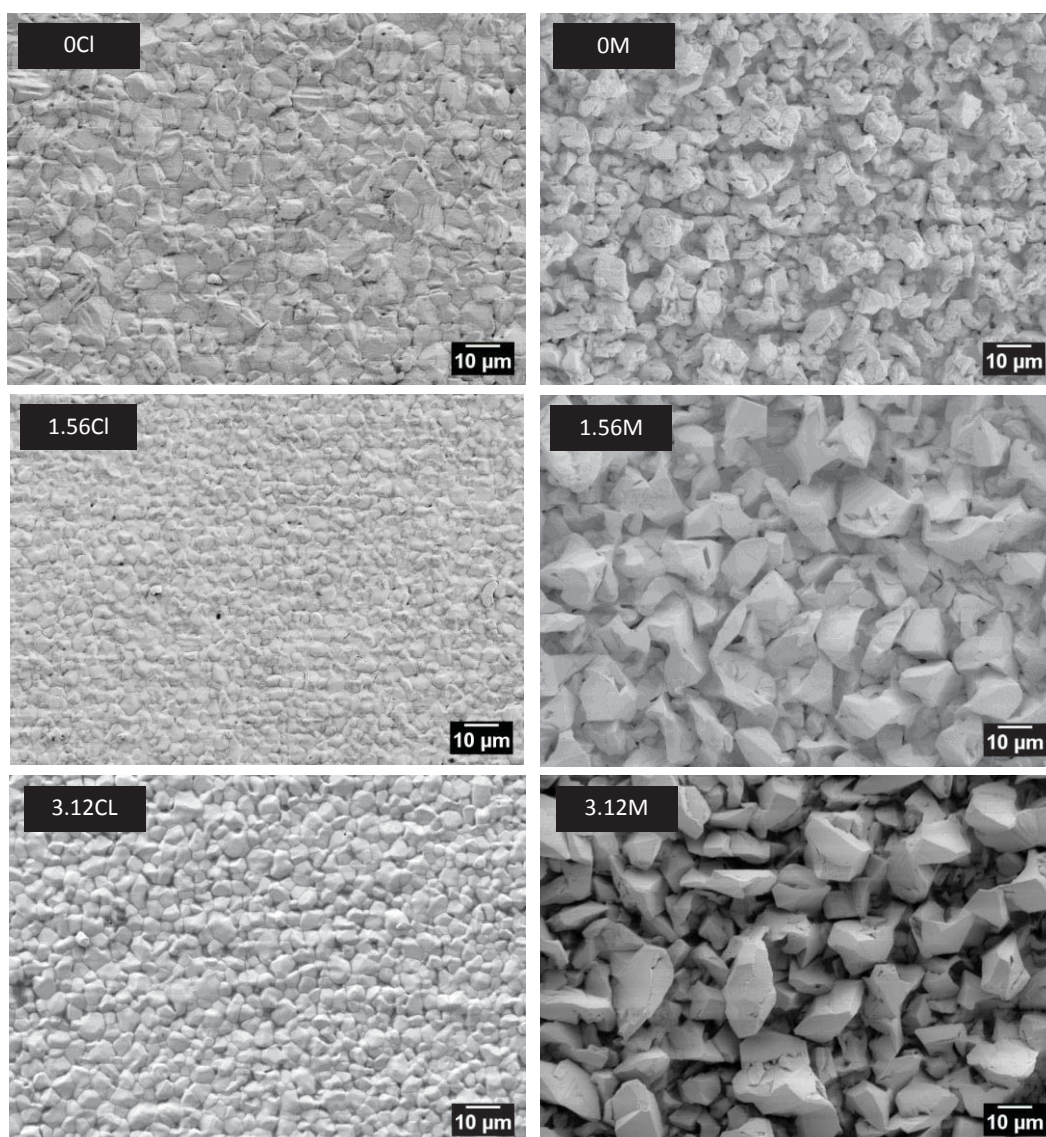
Figure 17: Polarization curves measured varying the ABN content in the chloride based electrolyte (a) and in the MSA electrolyte (b).

Table 3: Influence of the ABN concentration on the exchange current density ( $J_0$ ) calculated from the Tafel measurements in both electrolytes.

ABN concentration (mg/l)	$J_0$ in chloride electrolyte (mA/cm <sup>2</sup> )	$J_0$ in MSA electrolyte (mA/cm <sup>2</sup> )
0	7.1	25.1
0.78	0.8	24
3.12	0.7	20.9

### 5.2.2 Additive effects on the Sn morphology and crystallographic orientation

SEM micrographs of the as-deposited tin coatings were acquired in order to investigate the influence of the concentration of ABN on the surface morphology. The results are presented in Fig. 18. As shown from the SEM micrographs, the addition of ABN leads to a change in the grain structure of the samples deposited from the chloride based electrolyte. Without ABN the surface of the tin film appears rough with grains characterized with sharps edges and with striations in the surface. In the samples deposited with the addition of ABN, the surface appears smooth and the grains turn to a more defined polygonised shape with distinguishable grain boundaries. The observed change in the grain structure is related to the inhibition effects provided by the ABN additive. When adding ABN, the grain size is also reduced. The average grain size of the coatings was estimated by use of the Heyn linear intercept method [62] and the results are presented in Table 5 of paper 3. Samples deposited from the MSA electrolyte show a different trend. Independently on ABN addition the surface appears rough, with a complex grains structure (see Fig. 18). Furthermore, the addition of ABN results in an increase of the average grain size. The stirring of the plating solutions is not influencing the overall surface morphology and the average grain size of the samples deposited from both electrolytes. A slight increase of the average grain size value is measured for some of the samples deposited from the stirred electrolytes and it is in accordance with previous findings [63].



*Figure 18: Surface topography of the samples deposited from non-stirred solution with increasing ABN concentration: 0, 1.56 and 3.12 mg/l, from chloride based electrolyte in the left column, and from MSA electrolyte in the right column.*

The different influence of ABN in the two electrolytes is also visible in the XRD results. The effect of ABN on the preferred crystal orientation of Sn films was studied on coatings deposited from both electrolytes, from a stationary plating solution, and with 3 different ABN concentrations: 0, 1.56 and 3.12 mg/l. To avoid the detection of the substrate peaks, the analysis was performed with a grazing incidence configuration that allows to reduce the information depth of the measurements (limited to  $\sim 250$  nm from the surface of the sample). The results of the XRD measurements are presented as 3D plots in Fig. 19. From the analysis of the XRD spectra, all the Sn films deposited from both electrolytes can be considered as random-textured. As a matter of fact, X-ray spectra of random-textured Sn coatings are commonly characterized by several minor peaks of high Miller-indexed planes [64]. Such random-textured Sn coatings are found when the deposition is performed at relatively low current density, which results in a slower film growth rate. High current density favors the deposition of textured Sn coatings,

commonly along low Miller-indexed planes such as (200) or (220) [64]. As also seen in previous studies on Sn deposited from chloride based and MSA based electrolytes, these textured coatings show weak or no diffraction peaks from higher Miller indexes planes. However, the spectra shown in fig. 19 are characterized by the same number of peaks independently of the ABN addition in both electrolytes. Nevertheless, a common trend is observed from the XRD measurements acquired: a constant decrease of the (101) intensity with increasing ABN concentration. The trend is clearly more pronounced in the case of the sample deposited from the chloride electrolyte. This finding supports the hypothesis of ABN acting as an inhibitor in both chloride and MSA electrolytes, but to a different extent.

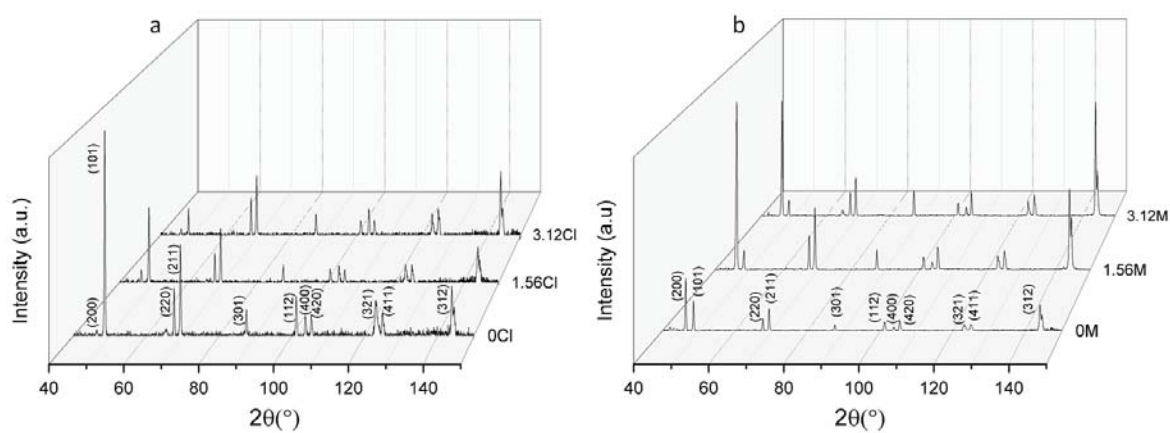


Figure 19: 3D X-ray diffraction profile of the Sn samples deposited from non-stirred chloride electrolyte with increasing ABN concentration (a), and of the Sn samples deposited from non-stirred MSA electrolyte (b).

## 6 Summary and Conclusions

The aim of this work was the characterization of electrodeposited Fe-based metallic coatings. Within this scope, characterization studies have been performed on Fe-W and Sn coatings. The characterization of the Sn coatings has been performed as a preliminary investigation to be then followed up by the deposition of binary and ternary Fe-Sn coatings.

Depending on the material under investigation, i.e Fe-W and Sn coatings, different research objectives were addressed. The objectives were described by the following research questions:

- When electrodepositing Fe-W alloys, what is the influence of the W content and of co-deposited impurities on the structure of the coatings?
- How are composition and structure influencing the hardness and thermal stability of the Fe-W coatings?
- Are the properties of the Fe-W coatings suitable for protective coating applications and other potential applications?
- When electrodepositing Sn coatings, what is the influence of the ABN additive on the two different electrolytes, i.e. chloride and MSA electrolytes?

For the Fe-W coatings it was found:

- The crystallographic structure of the Fe-W coatings changes with increasing the W content: a nanocrystalline structure is found for the 4 at.% W sample, a mixed nanocrystalline-amorphous structure for the sample with 16 at.% W, and a fully amorphous structure for the 24 at.% W sample.
- The presence of co-deposited C and O impurities lead upon annealing to the formation of phase not expected from the Fe-W diagram.  $\text{Fe}_6\text{W}_6\text{C}$  and  $\text{Fe}_3\text{W}_3\text{C}$  carbide phases were found for the alloys having 16 and 24 at.% of W.  $\text{FeWO}_4$  was found in the samples with 4 at.% and 16 at.% of W. However, as shown by combined XRD and EBSD results, longer annealing treatments result in the crystallization of stable phases as expected from the Fe-W binary phase diagram. This is observed with the gradual dissolution of the carbide phases and the crystallization of the  $\text{Fe}_2\text{W}$  phase.
- The thermal stability of Fe-W alloys increases with the W content: the Fe-W sample with 24 at.% W retains the amorphous structure up to 600 °C, where a partially crystalline structure was observed. Even after 12 hours annealing at 800 °C, the material is not fully crystalline.
- The annealing treatments improved considerably the hardness of the as-deposited Fe-W samples. The maximum hardness of 16.5 GPa was measured for the sample with 24 at.% of W after annealing for one hour at 600 °C and was related to the precipitation of fine  $\alpha$ -Fe crystallites.
- The obtained results regarding the thermal stability and hardness of the Fe-W sample with 24 at.% of W suggests that Fe-W coatings with high W content (i.e. >23 at.%) can be applied as a possible candidate for elevated-temperature applications.

For the Sn coatings it was found:

- In the chloride electrolyte, ABN acts as a highly effective inhibitor. Polarization measurements showed that increasing the concentration of ABN lead to a decrease in the cathode current density and the suppression of H<sub>2</sub> evolution is observed. The same trend is not observed in the polarization measurements from the MSA electrolyte. The different inhibition strength of ABN in the two electrolytes was also confirmed by the Tafel measurements. In both electrolytes the addition of ABN reduces the exchange current density but in the case of MSA electrolyte higher ABN concentrations are needed.
- ABN addition modifies the grain structure of the Sn samples deposited from the chloride based plating solution: smooth surfaces are obtained with well distinguishable grains of polygonal shape, and the average grain size is reduced. A different trend is instead observed for the Sn samples deposited from the MSA electrolyte. Independent of the ABN addition, the surface of samples appears rough, with a complex grains structure. Also, the addition of ABN results in an increase of the average grain size.
- The X-ray diffraction analyses show no clear texture development in the samples deposited from both electrolytes with ABN addition. However, a constant decrease of the (101) intensity is observed with increasing concentration of ABN. The trend is clearly more pronounced in the case of the sample deposited from the chloride electrolyte.

## 7 Future work

The thermal stability and the hardness of Fe-W coatings has been studied and is described in paper 1 and 2. Other properties such as wear and corrosion resistance are important for protective coating materials. Hence, it would be of interest to assess the wear performance and the corrosion resistance of Fe-W coatings. In paper 2, it has been shown that it is possible to enhance the hardness of the coatings by means of thermal treatments. Another interesting study would be the analysis of other ways to improve the wear and corrosion properties of the Fe-W coatings, e.g. the inclusion of reinforcing particles and the use of a third alloying element, respectively.

Regarding the work done on electrodeposited Sn, the results obtained in paper 3 show that the chloride-based electrolyte is more suitable to be optimized for the deposition of Fe-Sn coatings. A study of the obtained magnetic properties would be of interest to assess the alloy's potential in magnetic applications.

The studied Fe-W and Sn coatings were deposited respecting the limitations posed by the sustainability concerns discussed in chapter 1.1. The first results obtained from the Fe-W coatings are promising. Hence, Fe-W coatings have the prospect to be applied as sustainable replacement of hard Cr coatings. However, in order to become a valid alternative, it will be crucial to assess corrosion and wear resistance of the Fe-W system.

## **8 Acknowledgment**

I would like to thank my supervisors and examiner prof. Uta Klement for always being present in helping and supporting my work. Thank you.

I would like to thank all my colleagues and friends from the SELECTA project, it has been a lot of fun travelling and working together. A special thank goes to Aliona and Simona and to all the other people that were involved in the experimental work and writing of the papers. Working together was great.

Furthermore, I would like to thank all my friends and colleagues here at the Department of Industrial and Materials Science. Especially my work-buddies Casey, Dmitri and Philipp. I would like to thank Dr. Eric Tam and Dr. Yiming Yao for their help regarding the experimental work here at the department such as electron microscopy and X-ray analysis.

Finally, I want to thank my brother Alberto, my mum and my father for their unconditioned love and support. Thank you always. Love you.

## 9 References

- [1] ASTM B374-06 Standard Terminology Relating to Electroplating, ASTM Int. (2011) 1–9. doi:10.1520/B0374-06R10.2.
- [2] M. Schlesinger, M. Paunovic, Modern Electroplating, 5th edition, John Wiley & Sons, Inc., 2010.
- [3] Y.D. Gamburg, G. Zangari, Theory and Practice of Metal Electrodeposition, 2011. doi:10.1017/CBO9781107415324.004.
- [4] A. Robertson, U. Erb, G. Palumbo, Practical applications for electrodeposited nanocrystalline materials, *Nanostructured Mater.* 12 (1999) 1035–1040. doi:10.1016/S0965-9773(99)00294-9.
- [5] U. Erb, K.T. Aust, G. Palumbo, Electrodeposited Nanocrystalline Metals, Alloys, and Composites, *Nanostructured Mater.* Second Ed. (2007) 235–292. doi:http://dx.doi.org/10.1016/B978-081551534-0.50008-7.
- [6] T. Osaka, M. Datta, Y. Shacham-Diamand, *Electrochemical Nanotechnologies*, Springer, 2010. doi:10.1007/978-1-4614-4605-7.
- [7] W. Clark, N. Dickson, Sustainability science: the emerging research program, *Proc. Natl. Acad. Sci.* 100 (2003) 8059–8061. <http://www.pnas.org/content/100/14/8059.short>.
- [8] U. Klement, E. Pellicer, J. Sort, Mid-term meeting of SELECTA: a European Training Network on smart electrodeposited alloys for environmentally sustainable applications, *Trans. IMF.* 95 (2017) 124–125. doi:10.1080/00202967.2017.1299307.
- [9] <http://echa.europa.eu/web/guest/regulations/reach/candidate-list-substances-in-articles> (accessed February 15, 2018).
- [10] S.K. Ghosh, J.P. Celis, Tribological and tribocorrosion behaviour of electrodeposited CoW alloys and CoW-WC nanocomposites, *Tribol. Int.* 68 (2013) 11–16. doi:10.1016/j.triboint.2012.08.012.
- [11] [http://europa.eu/rapid/press-release\\_IP-13-658\\_en.htm](http://europa.eu/rapid/press-release_IP-13-658_en.htm) (accessed February 15, 2018).
- [12] <http://ec.europa.eu/growth/sectors/raw-materials/specific-interest/critical/> (accessed February 15, 2018).
- [13] <http://www.un.org/sustainabledevelopment/> (accessed February 15, 2018).
- [14] <http://selecta-etn.eu/project> (accessed February 15, 2018).
- [15] Y. Zhang, Tin and Tin Alloys for Lead-Free Solder, *Mod. Electroplat.* Fifth Ed. (2011) 139–204. doi:10.1002/9780470602638.ch6.
- [16] H. Fischer, Wirkungen der Inhibitoren bei der Elektrokristallisation, *Electrochim. Acta*. 2 (1960) 50–96.
- [17] H. Fischer, Electrocrystallization of Metals under Ideal and Real Conditions, *Angew. Chemie Int. Ed. English.* 8 (1969) 108–119. doi:10.1002/anie.196901081.
- [18] E. Bauer, Phänomenologische Theorie der Kristallabscheidung an Oberflächen. I, *Zeitschrift Für Krist.* 110 (1958) 372–394.

- [19] H. Fischer, *Elektrolytische Abscheidung und Elektrokristallisation von Metallen*, Springer, Berlin, 1954.
- [20] R. Winand, *Electrocrystallization - theory and applications*, *Hydrometallurgy*. 29 (1992) 567–598. doi:10.1016/0304-386X(92)90033-V.
- [21] U. Erb, A.M. El-Sherik, G. Palumbo, K.T. Aust, *Synthesis, structure and properties of electroplated nanocrystalline materials*, *Nanostructured Mater.* 2 (1993) 383–390.
- [22] G. Palumbo, S.J. Thorpe, K.T. and Aust, *On the contribution of triple junctions to the structure and properties of nanocrystalline materials*, *Scr. Metall. Mater.* 24 (1990) 1347–1350.
- [23] R. Scully, A. Gebert, J.H. Payer, *Corrosion and related mechanical properties of bulk metallic glasses*, *J. Mater. Res.* 22 (2007) 302–313. doi:10.1557/jmr.2007.0051.
- [24] M.L. Holt, R. and Black, *Electrodeposition of iron-tungsten alloys from an acid plating bath*, *J. Electrochem. Soc.* 82 (1942) 205–215.
- [25] M.H. Lietzke, M.L. and Holt, *Codeposition of tungsten and iron from aqueous ammoniacal citrate bath*, *J. Electrochem. Soc.* 94 (1948) 252.
- [26] N. Tsyntaru, H. Cesiulis, M. Donten, J. Sort, E. Pellicer, E.J. Podlaha-Murphy, *Modern trends in tungsten alloys electrodeposition with iron group metals*, *Surf. Eng. Appl. Electrochem.* 48 (2013) 491–520. doi:10.3103/S1068375512060038.
- [27] M. Donten, *Bulk and surface composition, amorphous structure, and thermocrystallization of electrodeposited alloys of tungsten with iron, nickel, and cobalt*, *J. Solid State Electrochem.* 3 (1999) 87–96. doi:10.1007/s100080050133.
- [28] M.X. Donten, H. Cesiulis, Z. Stojek, *Electrodeposition and properties of Ni-W, Fe-W and Fe-Ni-W amorphous alloys. A comparative study*, *Electrochim. Acta.* 45 (2000) 3389–3396. doi:10.1016/S0013-4686(00)00437-0.
- [29] C.G. Vayenas, R.E. White, M.E. Gamboa-Aldeco, *Modern Aspects of Electrochemistry*, Vol. 42, Springer, 2008.
- [30] Z.I. Bobanova, A.I. Dikumar, H. Cesiulis, J.-. P. Celis, N.I. Tsyntaru, I. Prosycevas, *Micromechanical and Tribological Properties of Nanocrystalline Coatings of Iron-Tungsten Alloys Electrodeposited from Citrate-Ammonia Solutions*, *Russ. J. Electrochem.* 45 (2009) 895–901. doi:10.1134/S1023193509080096.
- [31] N.I. Tsyntaru, Z.I. Bobanova, D.M. Kroitoru, V.F. Cheban, G.I. Poshtaru, A.I. Dikumar, *Effect of a multilayer structure and lubrication on the tribological properties of coatings of Fe-W alloys*, *Surf. Eng. Appl. Electrochem.* 46 (2010) 538–546. doi:10.3103/S1068375510060025.
- [32] S. Wang, C. Zeng, Y. Ling, J. Wang, G. Xu, *Phase transformations and electrochemical characterizations of electrodeposited amorphous Fe–W coatings*, *Surf. Coatings Technol.* 286 (2016) 36–41. doi:10.1016/j.surfcoat.2015.12.011.
- [33] B. Morgan, O. and Lahav, *The effect of pH on the kinetics of spontaneous Fe(II) oxidation by O<sub>2</sub> in aqueous solution--basic principles and a simple heuristic description.*, *Chemosphere.* 68 (2007) 2080.
- [34] Y.D. Gamburg, E.N. Zakharov, G.E. Goryunov, *Electrodeposition, Structure, and Properties of Iron–Tungsten Alloys*, 37 (2001) 670–673.

- [35] A. Nicolenco, N. Tsyntaru, H. Cesiulis, Fe (III)-Based Ammonia-Free Bath for Electrodeposition of Fe-W Alloys, *J. Electrochem. Soc.* 164 (2017) D590–D596. doi:10.1149/2.1001709jes.
- [36] A. Nicolenco, N. Tsyntaru, J. Fornell, E. Pellicer, J. Reklaitis, D. Baltrunas, H. Cesiulis, J. Sort, Mapping of magnetic and mechanical properties of Fe-W alloys electrodeposited from Fe(III)-based glycolate-citrate bath, *Mater. Des.* 139 (2018) 429–438. doi:10.1016/j.matdes.2017.11.011.
- [37] Y. Nishi, Y. Mogi, K. Oguri, T. Watanabe, Preparation of Fe-W amorphous films by an electroplating method, *J. Mater. Sci. Lett.* 20 (1995) 1–3.
- [38] M.C. Chou, C.F. Chu, S.T. Wu, Phase transformations of electroplated amorphous iron-tungsten-carbon film, *Mater. Chem. Phys.* 78 (2003) 59–66. doi:10.1016/S0254-0584(02)00217-1.
- [39] N. Tsyntaru, J. Bobanova, X. Ye, H. Cesiulis, A. Dikumar, I. Prosycevas, J.P. Celis, Iron-tungsten alloys electrodeposited under direct current from citrate-ammonia plating baths, *Surf. Coat. Technol.* 203 (2009) 3136–3141. doi:10.1016/j.surfcoat.2009.03.041.
- [40] E.P. Barbano, I.A. Carlos, E. Vallés, Electrochemical synthesis of Fe-W and Fe-W-P magnetic amorphous films and Fe-W nanowires, *Surf. Coatings Technol.* 324 (2017) 80–84. doi:10.1016/j.surfcoat.2017.05.071.
- [41] F.C. Walsh, C.T.J. Low, A review of developments in the electrodeposition of tin, *Surf. Coatings Technol.* 288 (2016) 79–94. doi:10.1016/j.surfcoat.2015.12.081.
- [42] G.I. Medvedev, N.A. Makrushin, Electrodeposition of Tin from Sulfate Electrolyte in the Presence of Syntanol, Formaldehyde, and Allyl Alcohol, *Russ. J. Appl. Chem.* 77 (2004) 1781–1785.
- [43] L.N. Bengoa, W.R. Tuckart, N. Zabala, G. Prieto, W.A. Egli, Tin Coatings Electrodeposited from Sulfonic Acid-Based Electrolytes: Tribological Behavior, *J. Mater. Eng. Perform.* 24 (2015) 2274–2281. doi:10.1007/s11665-015-1503-4.
- [44] C. Rosenstein, Methane Sulfonic Acid as an Electrolyte for Tin, Lead and Tin-Lead Plating for Electronics, *Met. Finish.* 19 Jan (1990) 17–21.
- [45] C.T.J. Low, F.C. Walsh, The stability of an acidic tin methanesulfonate electrolyte in the presence of a hydroquinone antioxidant, *Electrochim. Acta.* 53 (2008) 5280–5286. doi:10.1016/j.electacta.2008.01.093.
- [46] C.T.J. Low, F.C. Walsh, Electrodeposition of tin, copper and tin–copper alloys from a methanesulfonic acid electrolyte containing a perfluorinated cationic surfactant, *Surf. Coatings Technol.* 202 (2008) 1339–1349. doi:10.1016/j.surfcoat.2007.06.032.
- [47] N.M. Martyak, R. Seefeldt, Additive-effects during plating in acid tin methanesulfonate electrolytes, *Electrochim. Acta.* 49 (2004) 4303–4311. doi:10.1016/j.electacta.2004.03.039.
- [48] R. Sekar, C. Eagammai, S. Jayakrishnan, Effect of additives on electrodeposition of tin and its structural and corrosion behaviour, *J. Appl. Electrochem.* 40 (2010) 49–57. doi:10.1007/s10800-009-9963-6.
- [49] A. Sharma, S. Bhattacharya, S. Das, K. Das, Influence of current density on surface morphology and properties of pulse plated tin films from citrate electrolyte, *Appl. Surf.*

- Sci. 290 (2014) 373–380. doi:10.1016/j.apsusc.2013.11.088.
- [50] Electrochemical Society (U.S.), *Modern electroplating* / edited by Frederick A. Lowenheim, 3th ed, Wiley, New York, 1974.
- [51] J.I. Goldstein, D.E. Newbury, P. Echlin, D.C. Joy, C.E. Lyman, E. Lifshin, L. Sawyer, J.R. Michael, *Scanning Electron Microscopy and X-ray Microanalysis*, Springer, 2005.
- [52] T. Maitland, S. Sitzman, *Electron Backscatterd Diffraction (EBSD) Technique and Materials Characterization Examples*, *Scanning Microsc. Nanotechnol. Tech. Appl.* (2007) 41–76. doi:0387396209.
- [53] A.J. Schwartz, M. Kumar, B.L. Adams, D.P. Field, *Electron Backscatter Diffraction in Materials Science*, 2009. doi:10.1007/978-0-387-88136-2.
- [54] P. Daab, E. Hornbogen: *Durchstrahlungs-Elektronenmikroskopie fester Stoffe*, Wiley-VCH Verlag GmbH & Co. KGaA, 1971. doi:10.1002/bbpc.19720760631.
- [55] W.C. Oliver, G.M. Pharr, Measurement of hardness and elastic modulus by instrumented indentation: Advances in understanding and refinements to methodology, *J. Mater. Res.* 19 (2004) 3–20. doi:10.1557/jmr.2004.19.1.3.
- [56] F. He, J. Yang, T. Lei, C. Gu, Structure and properties of electrodeposited Fe-Ni-W alloys with different levels of tungsten content: A comparative study, *Appl. Surf. Sci.* 253 (2007) 7591–7598. doi:10.1016/j.apsusc.2007.03.068.
- [57] A. Antoni-Zdziobek, T. Commeau, J.M. Joubert, Partial redetermination of the Fe-W phase diagram, *Metall. Mater. Trans. A Phys. Metall. Mater. Sci.* 44 (2013) 2996–3003. doi:10.1007/s11661-013-1658-2.
- [58] A. Jacob, C. Schmetterer, L. Singheiser, A. Gray-Weale, B. Hallstedt, A. Watson, Modeling of Fe-W phase diagram using first principles and phonons calculations, *Calphad Comput. Coupling Phase Diagrams Thermochem.* 50 (2015) 92–104. doi:10.1016/j.calphad.2015.04.010.
- [59] S.-J. Mun, M. Kim, T.-H. Yim, J.-H. Lee, T. Kang, Mechanical and Structural Characteristics of Electrodeposited Ni-Fe-W Alloy after Heat-Treatment, *J. Electrochem. Soc.* 157 (2010) D177–D180. doi:10.1149/1.3292282.
- [60] K. Hou, Y. Chang, S. Chang, C. Chang, The heat treatment effect on the structure and mechanical properties of electrodeposited nano grain size Ni – W alloy coatings, *Thin Solid Films.* 518 (2010) 7535–7540. doi:10.1016/j.tsf.2010.05.041.
- [61] C.J. Marvel, D. Yin, P.R. Cantwell, M.P. Harmer, The influence of oxygen contamination on the thermal stability and hardness of nanocrystalline Ni-W alloys, *Mater. Sci. Eng. A.* 664 (2016) 49–57. doi:10.1016/j.msea.2016.03.129.
- [62] E112-12: Standard Test Methods for Determining Average Grain Size, *ASTM Int.* (2012) 1–27. doi:10.1520/E0112-12.1.4.
- [63] S. Wen, J.A. Szpunar, Nucleation and growth of tin on low carbon steel, *Electrochim. Acta.* 50 (2005) 2393–2399. doi:10.1016/j.electacta.2004.10.053.
- [64] P. Jagtap, P. Kumar, Manipulating Crystallographic Texture of Sn Coatings by Optimization of Electrodeposition Process Conditions to Suppress Growth of Whiskers, *J. Electron. Mater.* 44 (2015) 1206–1219. doi:10.1007/s11664-014-3622-3.